

Thesis 367

Interferometric Synthetic Aperture Radar For Track Condition Monitoring

Case Study on Malmbanan

Kara Åmerbilly

Trafik och Väg
Institutionen för Teknik och Samhälle
Lunds Tekniska Högskola
Lunds Universitet



Copyright © Kara Åmerbilly

LTH, Institutionen för Teknik och samhälle
CODEN: LUTVDG/(TVTT-5334)/1-64 /2021
ISSN 1653-1922

Tryckt i Sverige av Media-Tryck, Lunds universitet
Lund 2021

Examensarbete

CODEN: LUTVDG/(TVTT-5334)/1-64
/2021

Thesis / Lunds Tekniska Högskola,
Institutionen för Teknik och samhälle,
Trafik och väg, 367

ISSN 1653-1922

Author(s): Kara Åmerbilly
Title: Interferometrisk Syntetisk aperturradar för underhållsmätningar av järnvägar. Fallstudie på Malmbanan
English title: Interferometric Synthetic Aperture Radar For Track Condition Monitoring. Case Study on Malmbanan
Language: English
Year: 2021
Keywords: InSAR; railway; maintenance; underhåll; järnväg
Citation: Åmerbilly, K., Interferometric Synthetic Aperture Radar For Track Condition Monitoring. Case Study on Malmbanan. Lund, Lunds universitet, LTH, Institutionen för Teknik och samhälle. Trafik och väg 2021. Thesis. 367

Abstract:

There is over 15,000 km of track in the Swedish railroad network. This network is vital for the transport of people and goods across the country. It is important that this network is monitored and maintained to ensure good function and safety. In recent decades the development of Interferometric Synthetic Aperture Radar (InSAR) and Time Series techniques has allowed researchers, geotechnicians and engineers to measure ground deformation over a large area remotely with high frequency and accuracy. The purpose of this study is to evaluate the use of InSAR technique for track condition monitoring and compare it to a conventional track condition monitoring techniques. The northern Malmbanan which is used to transport iron ore from Kiruna mines to ports Narvik in Norway was used as a case study for this project. Coordinate matching of measurements from the provided Small Baseline Subset (SBAS) InSAR data and Optram data from survey trains was performed. Then measured changes over different time spans in the two systems were overlapped and classified with different thresholds to see if there is correlation between the two systems. The results from the classification showed that there was too much variation in correlation to draw a clear conclusion about the use of InSAR for track condition monitoring. The SAR data which was captured with the Sentinel 1A/B constellation lacks the resolution or coherence to be practically useful for track condition monitoring.

Trafik och väg
Institutionen för Teknik och samhälle
Lunds Tekniska Högskola, LTH
Lunds Universitet
Box 118, 221 00 LUND

Transport and Roads
Department of Technology and Society
Faculty of Engineering, LTH
Lund University
Box 118, SE-221 00 Lund, Sweden

Abstract

There is over 15,000 km of track in the Swedish railroad network. This network is vital for the transport of people and goods across the country. It is important that this network is monitored and maintained to ensure good function and safety. In recent decades the development of Interferometric Synthetic Aperture Radar (InSAR) and Time Series techniques has allowed researchers, geotechnicians and engineers to measure ground deformation over a large area remotely with high frequency and accuracy.

The purpose of this study is to evaluate the use of InSAR technique for track condition monitoring and compare it to a conventional track condition monitoring techniques. The northern Malmbanan which is used to transport iron ore from Kiruna mines to ports Narvik in Norway was used as a case study for this project. Coordinate matching of measurements from the provided Small Baseline Subset (SBAS) InSAR data and Optram data from survey trains was performed. Then measured changes over different time spans in the two systems were overlapped and classified with different thresholds to see if there is correlation between the two systems.

The results from the classification showed that there was too much variation in correlation to draw a clear conclusion about the use of InSAR for track condition monitoring. The SAR data which was captured with the Sentinel 1A/B constellation lacks the resolution or coherence to be practically useful for track condition monitoring.

Sammanfattning

Järnvägsnätet i Sverige är över 15000 km långt. Järnvägsnätverket har en viktig roll i transporten av personer och gods i landet. Det är viktigt att övervaka och underhålla detta stora nätverk för att säkerställa god funktion och säkerhet. De senaste årtionden har utvecklingen av interferometriska syntetiska aperturradar (InSAR) och tidsserie tekniker lett till att forskare, geotekniker och ingenjörer kan fjärrmäta markdeformationer över stora områden med hög noggrannhet och frekvens.

Syftet med denna studien är att undersöka om InSAR kan användas för konditions- mätning av järnvägen och jämföra det med konventionella konditionsmättnings metoder. Malmbanan i norra Sverige som används för att transportera järnmalm från Kiruna till Narvik i Norge var fallstudie för detta projektet. Koordinat matchning av SBAS (Small baseline subset) InSAR mättningsdata med mättningsdata från Optram insamlat med mätningståg utfördes. Därefter överlappades uppmätta förändringar över olika tidsintervall i de två systemen och klassificerades med olika trösklar för att se om det finns en korrelation mellan de två systemen.

Resultaten från klassificeringen visade att variation i korrelationen var för stor för att dra en tydlig slutsats om användningen av InSAR för konditionsmätning av järnvägen. SAR data som samlades in med Sentinel 1A/B konstellationen har för låg upplösningen och koherensen för att vara praktiskt användbar för konditionsmätningar.

Foreword

I would like to thank my supervisors Carl-William Palmqvist and Sadegh Jamali at the faculty of engineering for guiding me through this process. I also want to thank the faculty at Luleå and Gävle university for providing insight and critique on this topic. I would also extend my gratitude towards staff at Trafikverket and Sweco for answering my questions and providing me with necessary data.

Innehåll

Contents	VIII
1 Introduction	1
1.1 Background	1
1.2 Problem statement	2
1.3 Research objectives	2
1.4 Limit of study	2
2 Theoretical background	3
2.1 InSAR	3
2.1.1 Active Radar	3
2.1.2 Synthetic Aperture Radar	4
2.1.3 Interferometric Synthetic Aperture Radar	6
2.1.4 Time Series InSAR	8
2.1.5 Application of InSAR	10
2.2 Conventional measuring methods - OPTRAM	11
2.3 Malmaban	13
3 Method	15
3.1 Data and methods	15
3.2 Understanding the raw data	17
3.2.1 InSAR data	17
3.2.2 Optram data	19
3.3 Preparing the data	21
3.4 Aggregate and matching points	23

3.5	Establishing threshold	26
3.6	Identify problematic areas	28
3.7	Overlap	29
3.8	Sensitivity analyst	31
4	Results and Analysis	33
4.1	Classification With Different Time Ranges	33
4.2	Classification With Different Thresholds and Section Lengths	35
5	Discussion	41
5.1	Effect of Time Frames	41
5.2	Selection of Thresholds	43
5.3	Aggregation Length	43
5.4	Sources of Error	44
5.5	Method discussion	45
6	Conclusion	47
6.1	Future research	47
7	References	49
7.1	Literature	49
7.2	Images	51

1 Introduction

1.1 Background

The railroads stability is crucial for operation, whether it is for passenger trains or freight trains (Chang et al, 2014). In order to monitor the condition of the railroad and ensure its performance, safety and reduce the life cycle cost (Yang, 2015), routine inspections must be made. Defects, deformations and settlements leads to increased risk for accidents and disturbances. Accidents like derailment could potentially have serious consequences for human lives and disturbances leads to delays, rerouting of trains or canceled trains (Chinowsky et al, 2019).

Conventional monitoring of railways involves in-situ methods, such as leveling or deployment of survey trains. These methods are often labor intensive, expensive and time consuming, and therefore only applied on a limited scale, in time and space. Additionally some in-situ monitoring methods can't be performed while the track is in use (Chang et al, 2014). Railways are a linear construction that covers large areas, they are in constant use and they subside continuously over time (Yang, 2015).

2020 is on track to be among the hottest year on record, with an average global temperature of 1.2 °C above the pre-industrial baseline (1850-1900). The raise in global average temperature is related to the emission of greenhouse gases into the atmosphere (IPCC, 2019). Other than higher global average temperatures, warming leads to increased number of extreme weather events, such as flooding, drought and wildfires. Since the emergence of railway as a mode of transport, operators and track owners have faced difficult environmental conditions that subjugate tracks, facilities and trains to a multitude of severe weather conditions (Rossetti, 2003). As the global average temperature, cold region become increasingly less cold while warm regions become more warm (Peterson, McGuirk, Houston, Horvitz & Wehner, 2008). Warmer temperatures contribute to rail buckling because of the thermal expansion of metal in the rail. Warmer temperatures also leads to thawing permafrost, as the near-permafrost melts the soil that the track has been built upon begins to subside. This causes disturbances for the railway and higher risks of accidents (Hjort et al, 2018).

Interferometric Synthetic Aperture Radar techniques (InSAR) can be applied to bypass the limits of conventional methods. InSAR can be used to detect changes in elevation on a millimeter scale with bi-weekly updates (Chang et al, 2014). Compared to conventional techniques, InSAR can cover large areas and can be operated remotely. InSAR can cost effectually monitor railways with out the need for specialized equipment or in-situ presence (Tosti et al, 2020). Prior research has proven InSAR a viable tool for monitoring topographic elevation and ground deformation. InSAR was first used in 1989 to measure ground deformation (Gabriel, 1989) and since then new methods and applications have been discovered.

1.2 Problem statement

Conventional measuring methods are time consuming, requires pre planning and are geographically limited. New techniques must be investigated for condition monitoring. Techniques that are practical, that can produce precise and consistent results. The Swedish rail network is over 15,000 km long therefore tools for analyzing this vast network must be researched.

1.3 Research objectives

The goal of this project is to research the possibility of utilizing InSAR for condition monitoring of the railway and compare it to the Optram method used by Trafikverket and evaluate it by practicality and consistency. Malmбанan in northern Sweden is case study for this research.

1.4 Limit of study

Only the section between Kiruna and border with Norway is part of the case study. Capturing of InSAR imagery and OPTRAM data will not be performed in this study, the relevant InSAR and OPTRAM data is provided to the author of the study. This study is limited to the height of the rail aspect of condition monitoring.

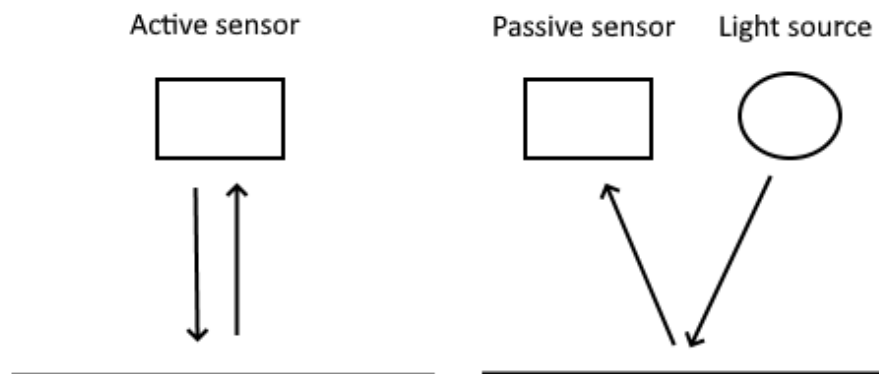
2 Theoretical background

This chapter start of by providing a general overview of how SAR measurements are gathered. The second part is about conventional railroad condition monitoring. Lastly a section is dedicated to the study area.

2.1 InSAR

2.1.1 Active Radar

An active radar sensor broadcast a known signal of electromagnetic energy to illuminate a spot on the Earth's surface, as seen in figure 2.1. When the energy hits the surface it scatters and some of this scatter returns to the broadcasting system. This is then registered and stored for further interpretation (Campbell Wynne, 2011) Unlike passive radars that rely on other sources for light energy for example the sun, active sensor generates its own light source thereby enabling it to operate day and night (Lillesand, Kiefer Chipman, 2014).

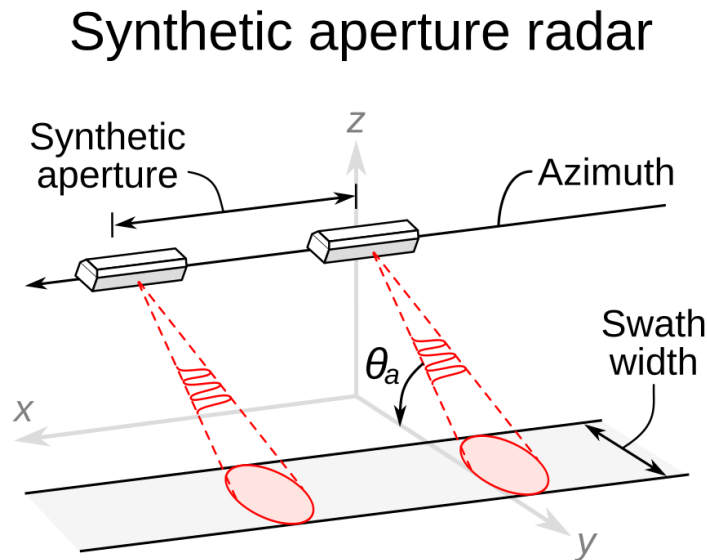


Figur 2.1: Active sensor generates its own light and is not dependent on a external light source

The active radar emits energy as microwaves, these exist on the electromagnetic spectrum between the length of about 1 millimeter to about 1 meter. There are two properties that makes microwave beneficial over visible wavelengths. The first is that microwave are able to operate under most weather conditions. The second property is that microwaves can penetrate clouds, rain, haze and smoke (Campbell Wynne, 2011; Lillesand, Kiefer Chipman, 2014)

2.1.2 Synthetic Aperture Radar

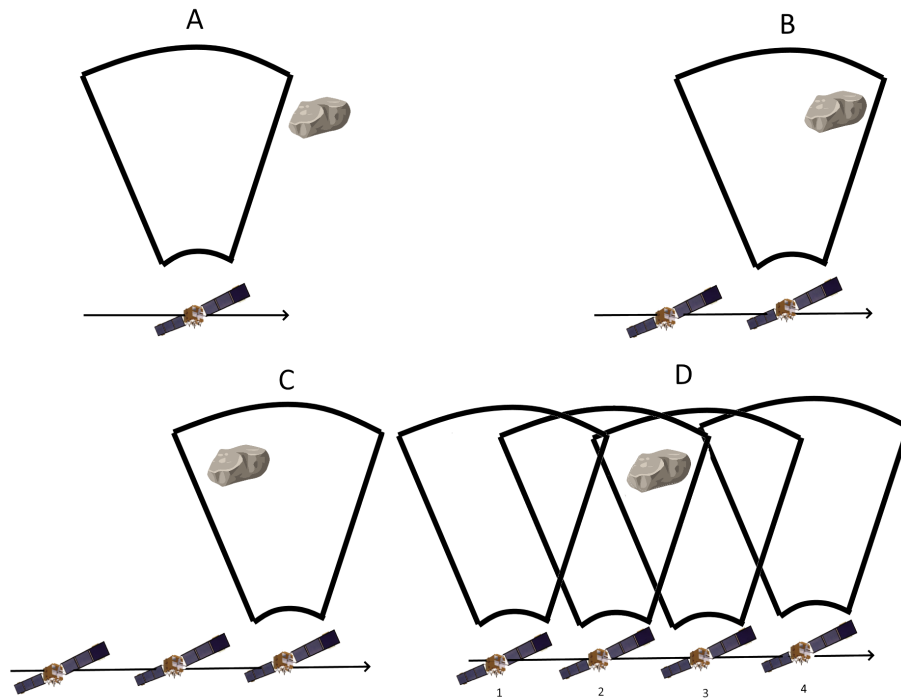
The active radar antennas on an airborne or a spaceborne platform broadcasts electromagnetic signals with high power in very short pulses at regular intervals to illuminate an area on the Earth's surface. When the transmitted microwaves reach the Earth's surface they get reflected of the surface or of a object existing on the surface. The reflected microwaves are then received by the antenna as backscatter (Lillesand, Kiefer Chipman, 2014). The typical frequency for the pulses range between from 100s to 1000s Hz for airborne and spaceborne systems. The area that can be illuminated varies from a few kilometers to 20 km for airborne systems and between 30 to 500 km for spaceborne systems (Moreira et al, 2013). A radar system that only uses one antenna for transmitting and receiving is called monostatic, whereas one that uses separate antennas for transmitting and receiving is called bistatic (Hanssen, 2002). Properties of the backscatter, such as amplitude and phase, depends on the physical and electrical properties of the imaged object (Ager, 2013). Until the 50s imaging radars were referred to as side looking airborne radar (SLAR). Azimuth resolution is the smallest separation between two objects that can be detected by the radar. For example a SLAR system with a 3 m antenna at 5 km range has an azimuth resolution of 50 m (Moreira et al, 2013). This low resolution has been the main disadvantage of side looking radar systems. In the 50s Synthetic aperture radar system were invented (SAR). For images captured with SAR the azimuthal resolution was equal to half the antenna length independent of range. A SAR system with a 3 m antenna at 5 km range the resolution would now become 1.5 m.



Figur 2.2: SAR platform moves in x direction and records backscatter from the swath. (RCraig09, 2020)

The azimuth (x) is the flight path of the platform and the ground range (y) is the direction that is perpendicular to the flight path (See figure 2.2). The swath width is the extent of the image in the ground range direction and the length is determined by distance traveled with the radar turned on. Consider figure 2.3. At A, the SAR imaging

system is positioned so that the object of interest is just outside the view of the radar. At B and C, the object is fully within the view of the radar. The system captures scatter from the object during B and C interval. At D, the different captured are added together. These positions are mathematically treated as if they were elements of a larger antenna (Campbell Wynne, 2011;Lillesand, Kiefer Chipman, 2014; Ager, 2013). As the distance between the system and the object increases more elements along the flight path can receive backscatter because of the conical shape of the imaging area. This means that the azimuth resolutions is constant and independent of range (Lillesand, Kiefer Chipman, 2014).



Figur 2.3: Different SAR phases. In the last frame D all the recorded scatter from the different phases are compiled

The received signal are stored as singel-look complexes (SLC), a SAR image where every pixel is corresponding to a resolution cell on the ground. These cells are sampled in azimuth and slant-range coordinate system. In the SLC format every cell has the complex P (Esfahany, 2017)

$$P = \text{Re}(P) + j\text{Im}(P) = A \cdot \exp(j\psi)$$

where A is the pixel amplitude which is the square root of the signal return intensity, j is the imaginary unit. ψ is the phase of the received signal. A and ψ are related to the real and imaginary part of P as

$$\text{Re}(P) = A \cdot \cos(\psi), \quad \text{Im}(P) = A \cdot \sin(\psi)$$

The phase ψ is consists of the four components

$$\psi = W\{\psi^{range} + \psi^{atmo} + \psi^{scat} + \psi^{noise}\}$$

W : modulo- 2π wrapping operator

ψ^{range} : Phase related to distance between cell on ground and position of radar sensor

ψ^{atmo} : Phase delay because of atmospheric effects

ψ^{scat} : Phase related to the distribution of scatterers within cell

ψ^{noise} : Phase due to system and thermal noise

2.1.3 Interferometric Synthetic Aperture Radar

Interferometric Synthetic Aperture Radar (InSAR) is a technique used to observe surface topography, subsidence, ground deformation and glacier movements (Moreira et al, 2013). By observing the phase difference between two SAR images, the information about the position of a target, or the displacement during the time between the acquisitions can be acquired (Esfahany, 2017). Several ways exist for gathering interferometric radar images, across-track or along-track. With across-track interferometry a moving platform equipped with a bi-static antennas that gathers radar data at the same time. By using two antennas it is possible to obtain distance and angular measurements. The principal is similar to how humans use two eyes for depth perception (Hanssen, 2002). Another method is along-track interferometry or differential interferometry where an radar platform passes over the study area two or more times. The image pairs can now reveal changes that have taken place between passes. In this case a temporal baseline is established. Short temporal baselines can collect more rapid movements, such as movement of ships, while long temporal baselines can measure movement of glaciers (Campbell Wynne, 2011). Differential interferometry can be operated from a bi-static platform with two antennas linearly along an orbital path or a mono-static platform in which a single antenna makes two or more orbits over the survey area (Yang, 2015; Campbell Wynne, 2011).

An InSAR image is created by interfering two SAR images taken from different positions or different times, where the phase difference between these two SAR images are of interest. As mentioned earlier ψ^{range} is related to the distance between the cell on the ground and the radar, therefore the phase difference between two SAR images can be exploited to calculate displacement between two acquisition times. The result of interfering two SAR images is another complex image called an interferogram. Because

of the fact that the two SAR images are acquired from two slightly different positions, it is required to align the geometry of one image to the other. Then a complex conjugate multiplication is performed on the aligned SAR images (Esfahany, 2017).

$$I = P_M P_S^* = A^M A^S \exp\left(j(W\{\psi_M - \psi_S\})\right)$$

I: Constructed interferogram

P_M : SAR master

P_S : SAR slave

*: Complex conjugate

For a single pixel the interferometric phase can be written as

$$\phi_{MS} = W\{\psi_M - \psi_S\} = W\{\phi^{range} + \phi^{atmo} + \phi^{scat} + \phi^{noise}\}$$

It is standard to explain phase by the degree of correlation between two SAR images, called coherence $|\gamma| \in [0, 1]$, where 0 means complete decorrelation and 1 means that robust deformation information can be generated. To generate accurate ground deformation it is generally required to have a coherence index above 0.5 (Yang, 2015).

The range dependent phase ϕ^{range} difference between the two SAR images is related to distance between the radar and the ground cell during the two acquisition times. This range dependent phase can be divided into three different categories.

$$\phi^{range} = \phi^{flat} + \phi^{topo} + \phi^{defo}$$

The flat phase is caused by the curved reference surface of the earth and depends on viewing angle. The topographic phase is the effect of the surface height above the reference surface. This also is dependent on the viewing angle. The deformation phase is caused by the surface deformation between the two acquisitions. The flat and topographic phases can be removed by using orbit parameters and an external digital elevation model (DEM). This leaves the phase caused by the surface displacement.

$$\phi^{atmo} = \phi_M^{atmo} - \phi_S^{atmo}$$

Changes in atmospheric conditions between two SAR acquisitions will result in different atmospheric phases. These atmospheric delays are caused by turbulent processes in the atmosphere and different vertical refractivity properties.

$$\phi^{scat} = \phi_M^{scat} - \phi_S^{scat}$$

The scattering phase is induced by difference in scattering behavior between two SAR acquisition. The scattering phase in each SAR image, is a function of the position of scatterers in a cell with respect to the radar and the electrical properties of the scatters. Decorrelation induced by scattering phase variation is divided into four categories. Baseline decorrelation is the result of different incidence angles between two SAR acquisitions. A ground cell on the ground seen by two radars at different angles will

give different phase information. Doppler centroid decorrelation is similar to baseline decorrelation in that they are both caused by difference in incidence angles. Volumetric decorrelation is caused by scattering in 3D volumes such as tree canopies. Temporal decorrelation is the result scatterer variation due to changes on the ground, such as vegetation growth or rainfall. The noise phase is the result of noise induced by the radar system and post-processing operations.

If the atmospheric, scattering and noise phase difference were zero, then a coherent image would be made and the interferometric phase would only depend on the change of travel time of the signal between sensor and pixel phase. But this is often not the case. The main challenge when using InSAR is the ability to extract coherent data from noisy interferometric phases. To manage the limitations of InSAR, a technique called time series InSAR was developed to manage decorrelation.

2.1.4 Time Series InSAR

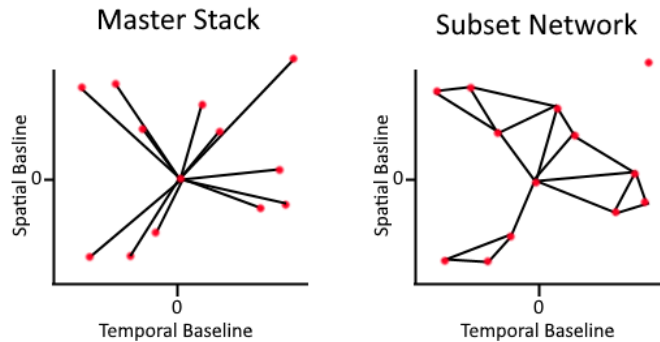
Time series techniques focus on tackling this decorrelation to produce deformation results (Minh, Hanssen Rocca, 2020). Two main approaches were developed. One to observe isolated pixels which do not suffer from decorrelation and then using these to extract deformation information. The other approach takes pixels affected by decorrelation and applies different filters and processes to reduce decorrelation. The first one is called the persistent scatterers interferometry (PSI) and the second is distributed scatterers interferometry (DSI) (Esfahany, 2017). There is also a combination of both. Due to the availability of historic SAR data it is possible to study temporal displacement over large time span by utilizing large stacks of SAR images. Figure 2.5 provides a simple flow chart for different types of InSAR techniques.

Persistent scatterer

For SAR images the value for each pixel is the sum of the returns from the scatterers on the ground. If these move in relation to each other between satellite passes then the phase return will vary randomly which causes decorrelation. If a pixel is instead dominated by one stable scatterer that has a high signal to noise-ratio, the variance becomes small enough to enable the extraction of deformation phase (Hooper, 2007). It only takes into consideration the phase information from stable backscatters in order to maintain coherence. This means that ϕ^{scat} is small over a large temporal and perpendicular baseline. This enables the extraction of information from a stack of interferograms. For PSI one image is chosen as master and all other images are referenced to it (Figure 2.4). Stable backscatterers can be buildings, bridges or large rocks. Stable backscatter are often refereed to as persistent scatterers (Yhokha et al, 2018).

Distributed scatterers

The idea behind distributed scatterers is to use interferogram pairs with minimal spatial and temporal baselines between acquisitions (Pawluszek-Filipaik Borkowski, 2020). DSI does not use single master stack (Figure 2.4). Instead they are arranged in subset network configurations. This reduces the decorrelation that occur with long baselines. Distributed scatterers technique is usually used when the surface is compromised of soil, vegetation and non-built-up areas (Minh, Hanssen Rocca, 2020).



Figur 2.4: Master stack for PSI and subset network for DSI

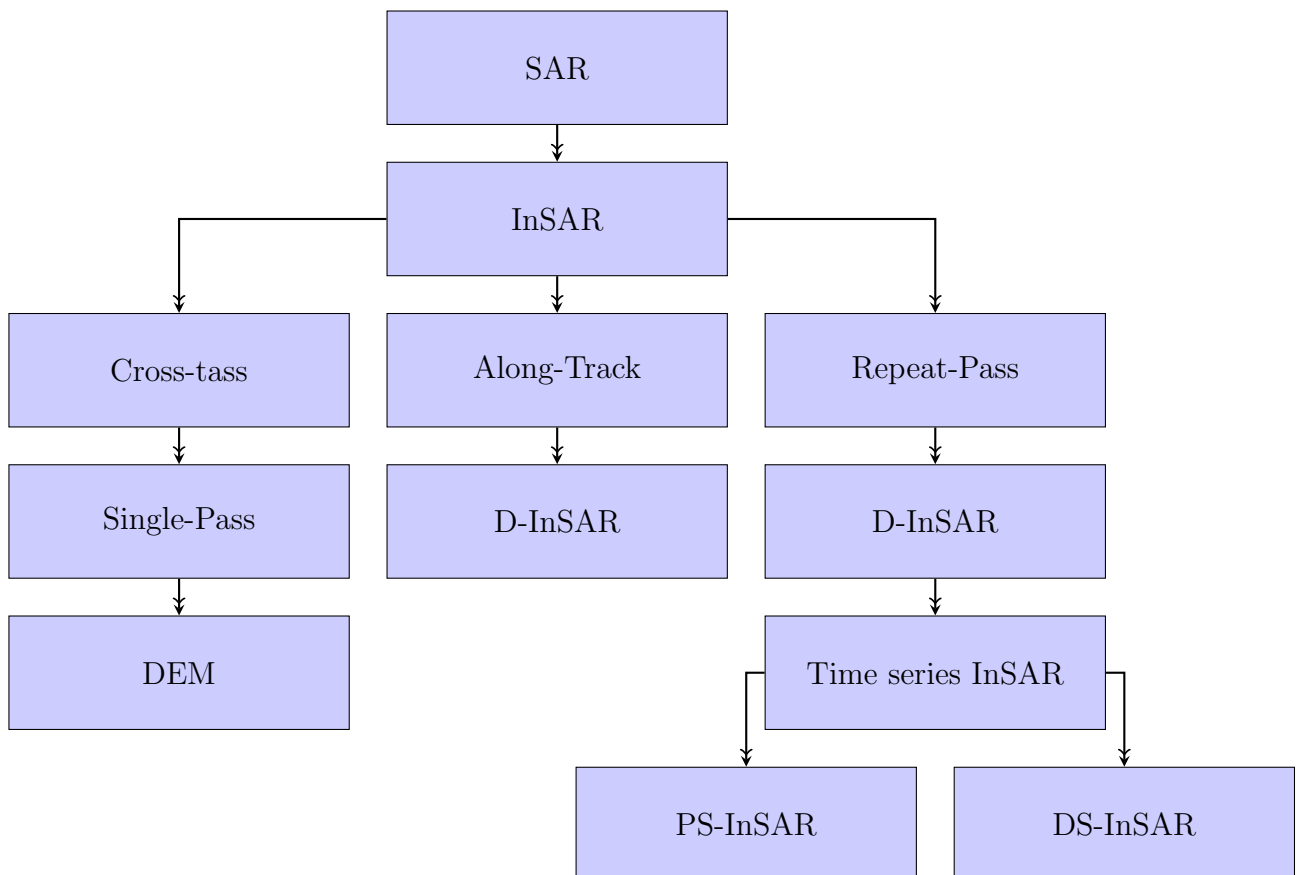


Figure 2.5: Simplified InSAR flow chart

2.1.5 Application of InSAR

Movement of tectonic plates and sub-tropical climate, has caused deformation of the slopes in the Himalaya region. Because of this deformation, landslides is an often occurring phenomenon, especially in the lesser Himalayan region. With high risk for disaster due to the geological instability and high population density, it becomes important to monitor the slopes to mitigate the risks. Yhokha et al. (2018) apply persistent scatterer interferometry to monitor the slope movements in the town Nainital in India. Utilizing PSI on 15 ENVISAT ASAR images captured from August 2008 to August 2010 they are able to reveal continuous creeping movements along the slopes.

Lauknes (2010) use InSAR to detect surface displacement in remote parts of Norway in order to map and monitor rockslides. Norway is a country with several thousands kilometers of populated coastlines and hillsides and monitoring all of them for hazards in a efficient manner is difficult. Conventional methods produce sparse and infrequent measurements. For this project they use SAR images from multiple satellites such as RADARSAT-2, ENVISAT ASAR and TerraSAR-X for their different resolutions and revisit times. This study demonstrate that InSAR have contributed to the understanding of the failure mechanism of multiple rockslides.

Giuqing and Jingqin (2008) describe land subsidence as a global problem and that conventional geodetic techniques are not suitable for large-scale monitoring. This applies time series InSAR to the Tianjin area in China to monitor land subsidence. By combining time series InSAR with PS technique they eliminated atmospheric delays. Images from the ENVISAT satellite was used in their experiment. They conclude that time series InSAR is a feasible and effective method for monitoring ground deformation.

Chang, Dollevoet and Hanssen (2014) conducted a study on the use of InSAR for railway monitoring. They survey a section freight railway in the Netherlands with 248 images from TerraSAR-X acquired between 2009 and 2013 of which 116 were ascending and 132 descending. Persistent scatterers are acquired from target with stable phase values such as buildings, rock and rails. They are able to observe significant deformation in the normal direction on long segments of the track (km) and at smaller hot-spots. They compare their results with in-situ survey train measurements to validate their results. Their conclusion was that detection and maintenance of railway track can be assisted by InSAR monitoring.

Yang (2015) applied InSAR to monitor and predict subsidence along a railway line in the United Kingdom. Yang utilized a time series permanent scatterer InSAR for monitoring subsidence and then developed three different methods for predicting future subsidence. Two statistical methods and one artificial neural network methods were used for prediction. They were able to measure land deformation velocity on a mm scale. For prediction they discovered that the artificial neural network method was best to predict future deformations.

2.2 Conventional measuring methods - OPTRAM

Attention for the geometric track quality arose in the middle of the 20th century. Different network owners started to develop their own monitoring systems. As the European countries started to integrate their rail networks it became necessary to compare track conditions across countries and networks, therefore new standards were developed (SS-EN 13848-1, 2019). In 2003 the first European standard for track quality measurement was approved. Since then updates and revisions have been made.

Currently railroad monitoring can be performed manually with leveling tools or with specialized survey trains. With manual tools, the track is measured without a traffic load (Trafikverket 2020a). While survey trains apply a load when measuring. The measuring of the Swedish railway system is performed by InfraNord which operates the IMV 100 and IMV 200 train that can measure the rail 1-6 times a year depending on the inspection class (Trafikverket, 2020). The survey train collects a large number of parameters about track position, rail profile, ballast profile, and overhead catenary system (Trafikverket, 2021a). The survey train measure while applying load to the track equivalent to a minimum 25 kN at wheel (SS-EN 13848-1, 2019). OPTRAM is the system used by Trafikverket to study and analyze measurements of track and overhead catenary line. The analysis is then used to plan maintenance works (Trafikverket, 2012a).

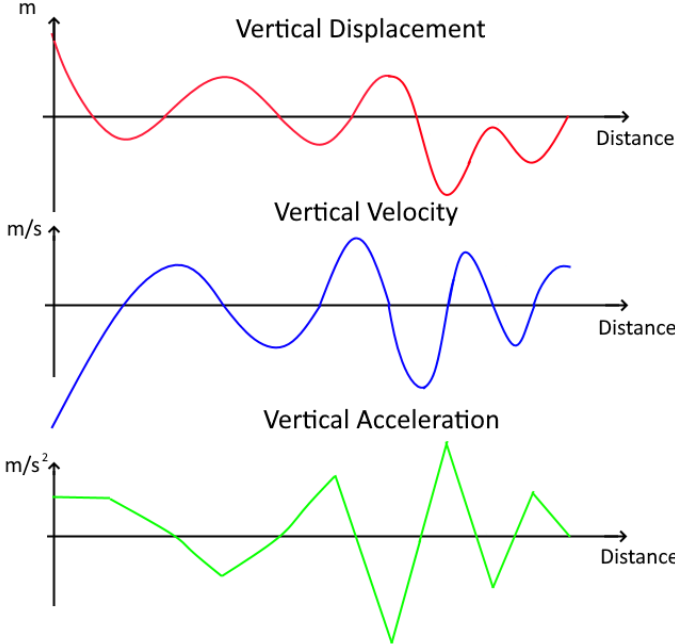
Measurements that are made are then compared to thresholds defined by Trafikverket to determine the condition of the railroad. There are four different threshold levels defined by Trafikverket (2020), these are ranked in their urgency for action. From low to high: PLAN, UH1, UH2 and KRIT. These levels are themselves derived from the SS-EN 13848 standard with slight modification. PLAN has the lowest urgency level and measurements that exceed this level should be considered for next maintenance operation. UH1 and UH2 are the next levels and defects over UH1 should be corrected before they reach UH2. Defects that exceed UH2, require immediate planing and maintenance should be performed without delay. Once KRIT has been reached immediate action is required, either immediate repair or risk reducing action such as lowering speed or stopping traffic.

TRVINFRA-00013	SS-EN 13848-5:2017
PLAN	Alert Limit (AL)
UH1	Intervention Limit
UH2	
KRIT	Immediate Action Limit

Figur 2.6: Difference between Trafikverket standard and SS-EN 13848 standard

The measured parameter of track geometry that is relevant for this project is longitudinal level. The survey trains are equipped with an accelerometer that measure the vertical acceleration of the train as it travels along the track. On track sections that are smooth and level, the accelerometer will not experience any vertical acceleration.

On the other hand sections that are undulating or contain rail defects, will cause the train to experience vertical acceleration. This vertical acceleration is then integrated twice to get vertical displacement (Figure 2.7). These vertical displacements are then compared to the thresholds specified by Trafikverket.



Figur 2.7: Relationship between vertical displacement of rail with vertical velocity and acceleration of train

2.3 Malmbanan

The railway that is of interest for this project is the railway from Kiruna in northern Sweden to Narvik in northern Norway. This section is located above the arctic circle where the mean temperature ranges between -14 C and $+14\text{ C}$ (SMHI, 2020). The railroad can be divided into three parts depending on prevailing soil type (Figure 2.8). The first part is comprised mostly of till and peat. This transitions into till and bare rock in the second section. The last third which is close to the Norwegian border is mostly rock. The soil depth gets as deep as 38 meters half way along the railroad according to data from the Geological Survey of Sweden (Figure 2.9). The railroad is primarily used to transport iron from the Swedish mines to the port at Narvik. It is a electrified single track rail way with a maximum axle load of 30 metric tons. It is the only railroad in Sweden with that load capacity. Between February 2019 and December 2020 test were made with axle loads of 32.5 metric tons. It is expected by Trafikverket (2021b) that longer and heavier trains will run on Malmbanan in the future and thus the performance requirements are getting higher.

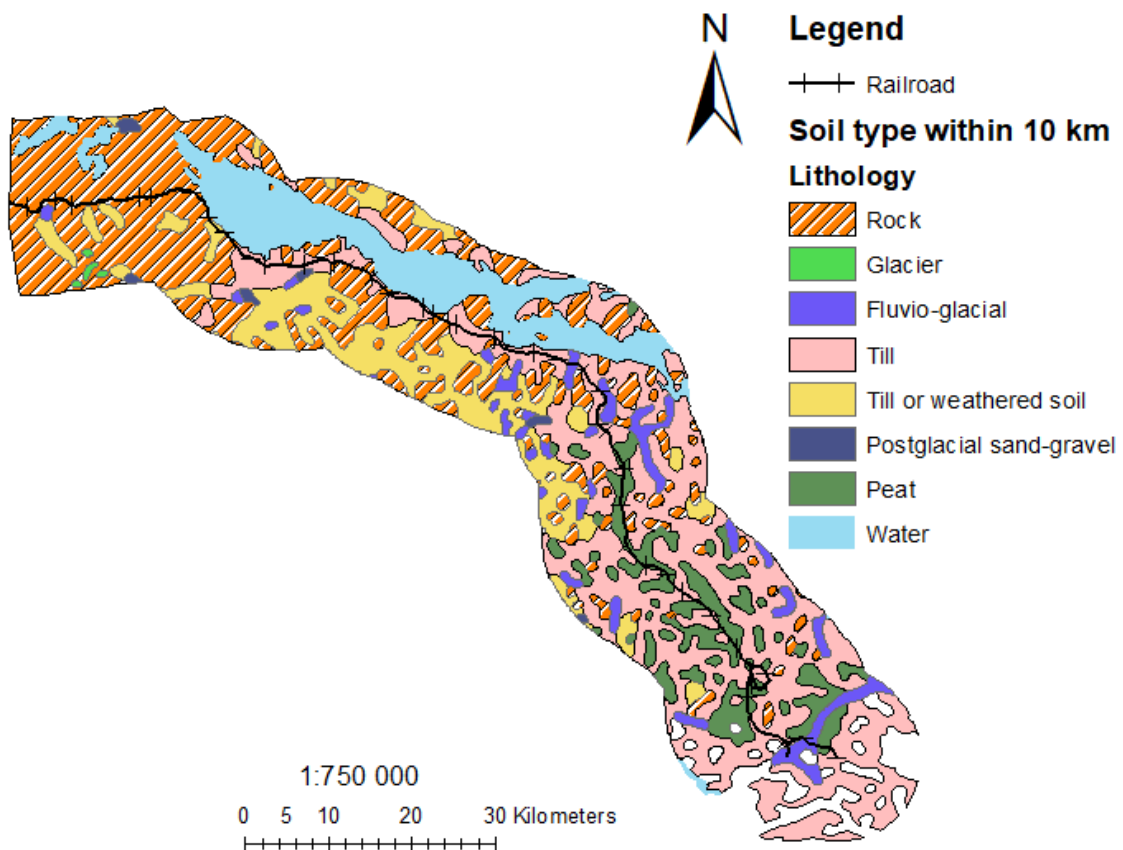
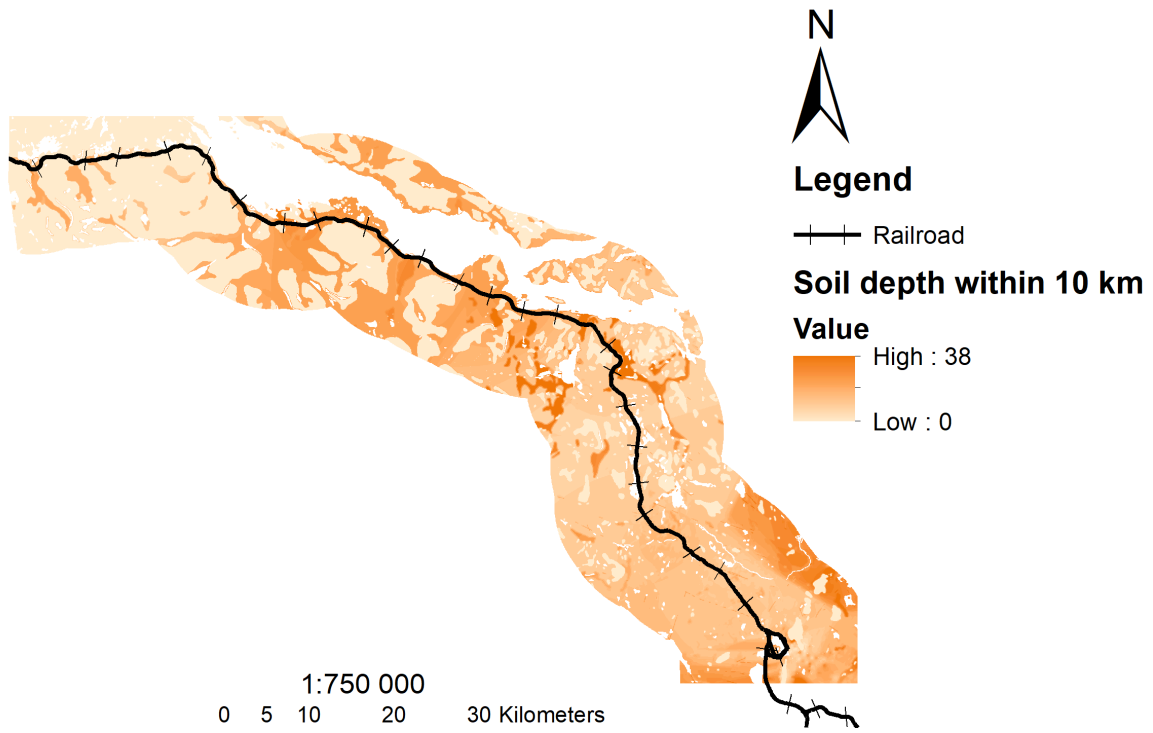


Figure 2.8: Soil types within 10 km distance to the railroad



Figur 2.9: Soil depth within 10 km distance to the railroad

3 Method

3.1 Data and methods

The aim of this project is to research the possibility of using interferometric synthetic aperture measuring methods (InSAR) for track condition monitoring. In order to reach a conclusion on whether InSAR can be used for this purpose, the methodology of this study will be about finding and analyzing factors and parameters that can be used to compare and contrast it with conventional monitoring techniques. For this research, quantitative comparison methods will be used to analyze the movements captured by InSAR measurement and Optram measurements.

It is not possible to directly compare the measurements from InSAR with those from Optram, because they measure different parameters in different ways. A method has to be developed to compare these two techniques. The first step is to understand the available data, how it is formatted and if there are any potential issues. From this data is then to select parameters that can be used to compare and analyze these two techniques. The second step is to aggregate and match the two data sets. The third step is to identify areas with significant changes over time in both Optram and InSAR. In the fourth step calculate the probability for overlap in changes for the two monitoring techniques. Lastly a sensitivity analysis is done to study how the selection of different parameters and thresholds effect the result. A flow chart visualizes the method in figure 3.3.

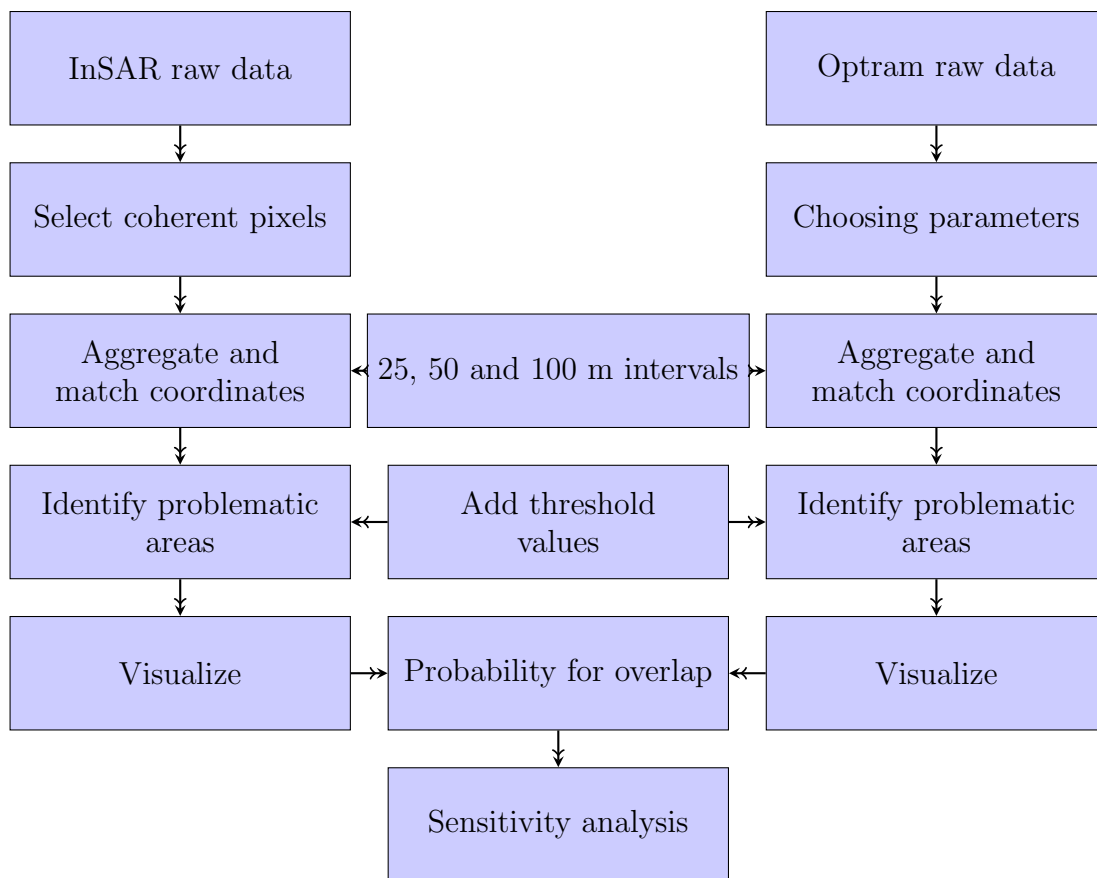
31 different tests will be performed. Seven tests with different time frames (Figure 3.1). Another 24 tests where four different time ranges are tested with six different parameters and thresholds (Figure 3.2). For the overlap analysis, a simple classification process will be deployed. This classification process will search for all the problematic areas identified by Optram and see if it overlaps with the problematic areas identified by InSAR.

	2015-12	2016-04	2017-04	2018-04	2019-04	2020-04	2020-06	Parameters
Test 1	1666 Days							50 meter, First Standard Deviation
Test 2	1174 Days							50 meter, First Standard Deviation
Test 3	365 Days							50 meter, First Standard Deviation
Test 4		365 Days						50 meter, First Standard Deviation
Test 5			365 Days					50 meter, First Standard Deviation
Test 6					365 Days			50 meter, First Standard Deviation
Test 7							90 Days	50 meter, First Standard Deviation

Figure 3.1: Seven test with different time frames

	2015-12	2020-06	Parameters		2016-04	2017-04	Parameters
Test 8			25 meter, First Standard Deviation	Test 14			25 meter, First Standard Deviation
Test 9			25 meter, Second Standard Deviation	Test 15			25 meter, Second Standard Deviation
Test 10			50 meter, First Standard Deviation	Test 16			50 meter, First Standard Deviation
Test 11			50 meter, Second Standard Deviation	Test 17			50 meter, Second Standard Deviation
Test 12			100 meter, First Standard Deviation	Test 18			100 meter, First Standard Deviation
Test 13			100 meter, Second Standard Deviation	Test 19			100 meter, Second Standard Deviation
	2017-04	2018-04	Parameters		2020-04	2020-06	Parameters
Test 20			25 meter, First Standard Deviation	Test 26			25 meter, First Standard Deviation
Test 21			25 meter, Second Standard Deviation	Test 27			25 meter, Second Standard Deviation
Test 22			50 meter, First Standard Deviation	Test 28			50 meter, First Standard Deviation
Test 23			50 meter, Second Standard Deviation	Test 29			50 meter, Second Standard Deviation
Test 24			100 meter, First Standard Deviation	Test 30			100 meter, First Standard Deviation
Test 25			100 meter, Second Standard Deviation	Test 31			100 meter, Second Standard Deviation

Figur 3.2: Four sets of six tests with the same time frame but different section lengths and thresholds



Figur 3.3: Method flowchart

3.2 Understanding the raw data

In this section a description of the data will be given. No collection of InSAR and Optram data was performed by the author of this thesis. Instead it was given in the form of very large spreadsheets. The raw data was collected by Trafikverket and Sweco.

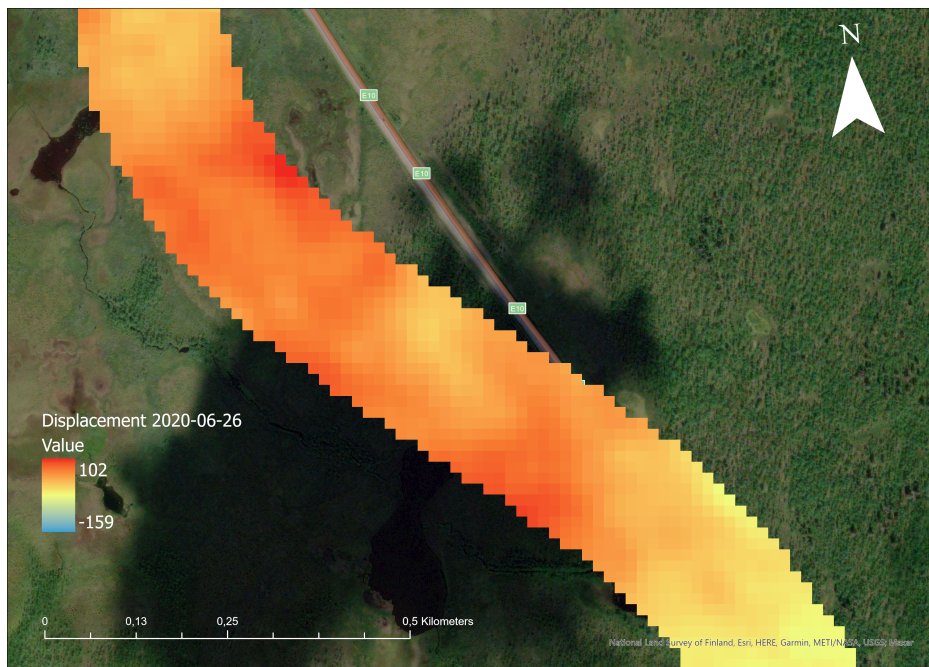
3.2.1 InSAR data

The original InSAR data was in spreadsheet form with about 500 000 rows and 240 columns (figure 3.4). Each row represents a measured ground cell in the area around the railroad, about 500 000 individual cells. Each cell contains information about its movement velocity, displacement over time, coherence, precision and location. The first measurement was performed 2015-09-27 and the last 2020-06-26. Between these two dates about 240 different measurements were made with varying time interval between each. The velocity was calculated as total displacement over the period divided by the length of the time period. For the displacement, the first measurement is counted as base level, which all other measurements are related to. The InSAR data were acquired with the Sentinel 1 constellation which is operated by the European space agency.

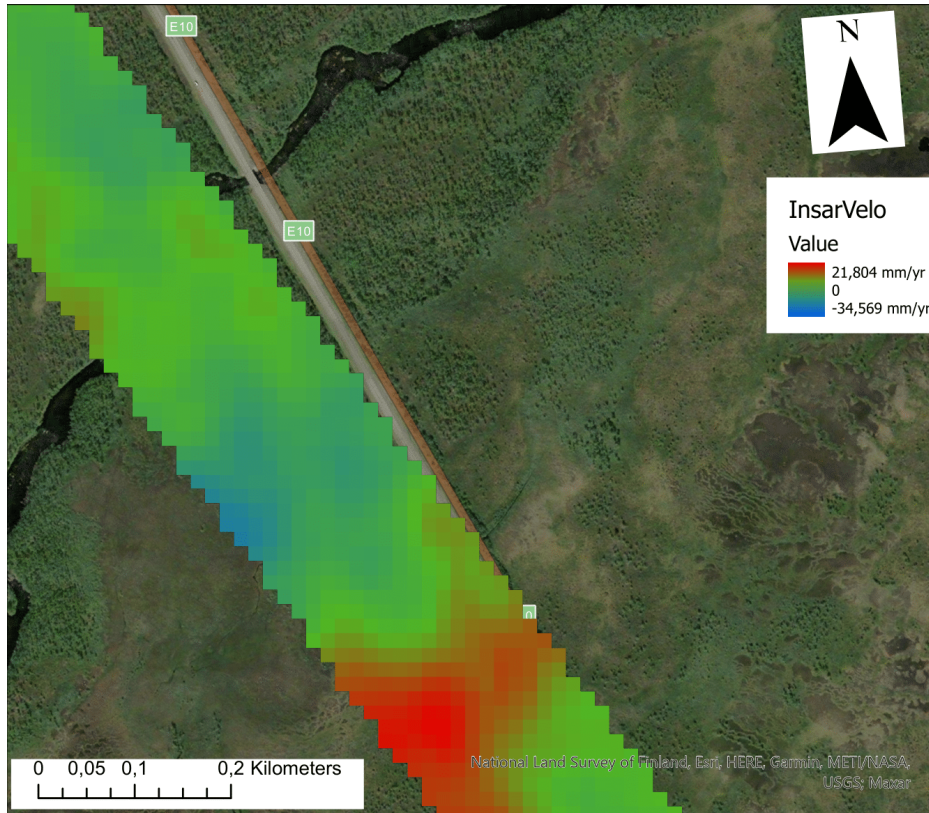


Figure 3.4: Raw InSAR data on the left. Visualization of each row in ArcGIS on the right

The cell can be visualized in a GIS environment and even converted to a raster for better understanding. In the figure 3.5 each cell represents the displacement in mm since first measurement and in figure 3.6 the vertical deformation velocity in mm per year. The raster has been clipped to only include cells within 100 meters on each side of the railway.



Figur 3.5: Cumulative vertical displacement in millimeter from start to end of measurements in a small area



Figur 3.6: Vertical displacement velocity in millimeter per year a small area.

3.2.2 Optram data

Similarly to the InSAR data, the Optram data was given in the form of multiple large spreadsheets. A total of 24 sets of data was given for the Optram data. Each set contained about 40 different collected measurements, some of which include the vertical alignment, horizontal alignment, track gauge, banking and cant. The provided measurements almost cover the whole distance between Kiruna and the border with Norway. These 24 data sets were spread over a time frame of five years and two months. Some years had up to six different measurements while other years only had three measurement. The time range for the Optram measurements was between 2015-04-06 and 2020-06-26. Each measured point is collected with assigned GPS coordinates and marker placement and offset. Markers are measured in kilometers from Stockholm. Offsets are measured in meters between markers. The Optram measurement can also be displayed in GIS software (Figure 3.7). In figure 3.8 vertical alignment for a 300 meter long section is plotted in Excel.



Figure 3.7: Optram data imported into GIS software. Here three measurement series from three different years are displayed.

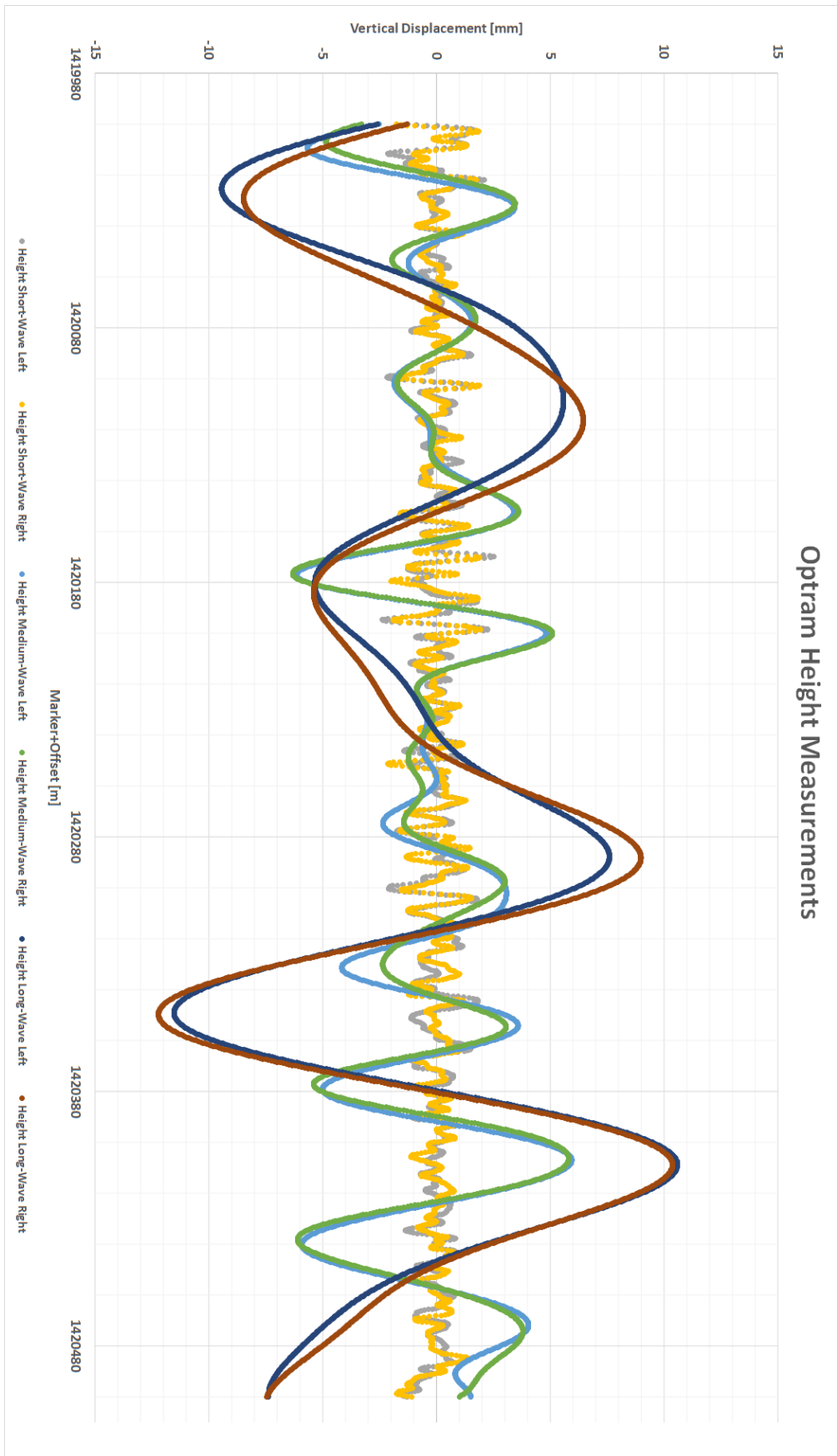
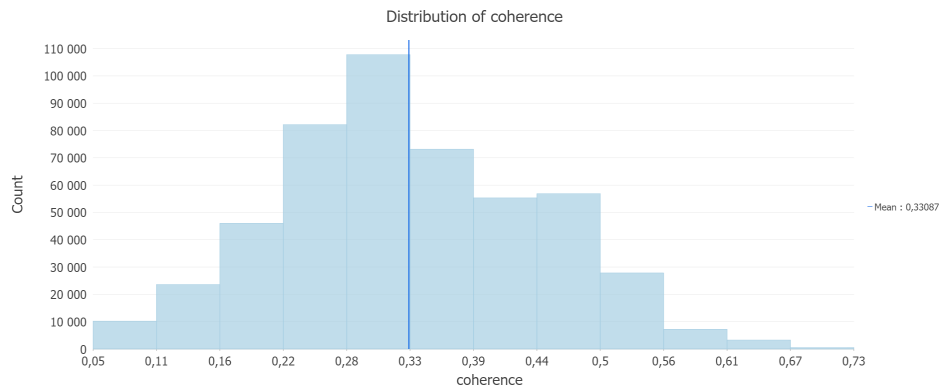


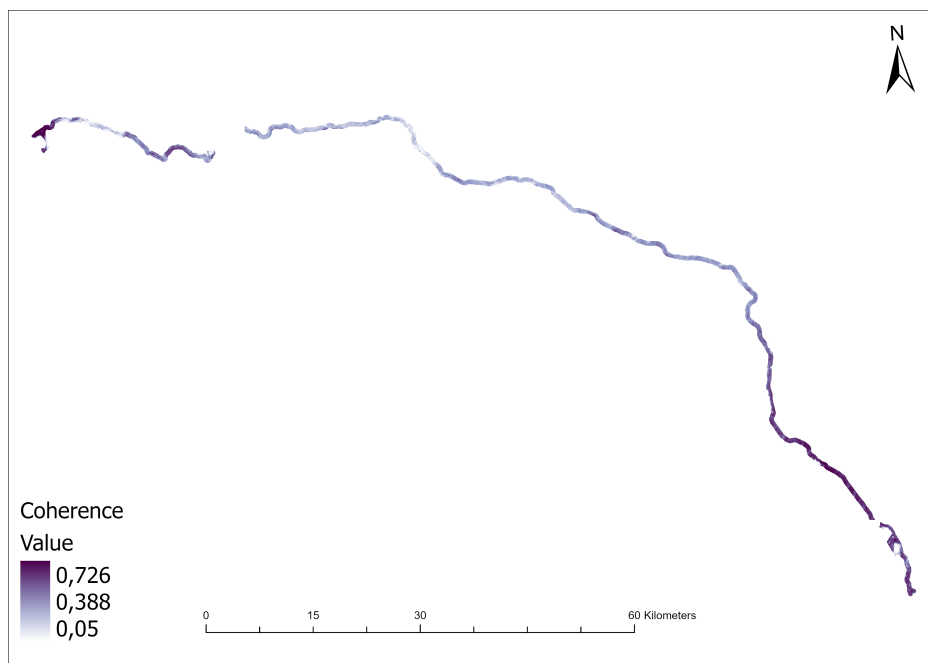
Figure 3.8: Optram measurements for a 300 meter section. Six curves for displacement for both rails in three wave lengths.

3.3 Preparing the data

As noted in sub chapter about interferometry. In order to generate accurate deformation results a coherence index above 0.5 is required. If we look at the coherence index of the pixels in the InSAR data set, we can see that the vast majority of them are below 0.5. Less then 8% of all the pixels have a coherence index above 0.5 (Figure 3.9). Further more the pixels that have coherence above 0.5 primarily located around Kiruna (Figure 3.11). We chose to only work with these pixels with coherence over 0.5 and exclude all other pixels.



Figur 3.9: Histogram of pixel coherence. Pixels with coherence lower than 0.5 are not usable for displacement monitoring.



Figur 3.10: Coherence of pixels on the railroad. The coherence is higher at the ends.

Not all parameters collected by Optram are relevant to this study. Only the parameters related to longitudinal level will be used.

- Height Short-wave Left (1-25 m)
- Height Short-wave Right (1-25 m)
- Height Medium-wave Left (25-70 m)
- Height Medium-wave Right (25-70 m)
- Height Long-wave Left (70-150 m)
- Height Long-wave Right (70-150 m)
- Standard Deviation Height
- Standard Deviation Interaction

3.4 Aggregate and matching points

The InSAR and Optram data set both contain GPS locations for every measurement this allows us to match these two sets. Because every Optram measurement comes with a marker location it is also possible to match measurements from different Optram series. In figure 3.12 we can see that multiple Optram measurement fit inside a single InSAR cell. Figure 3.13 gives an overview for how the two data sets are merged into one data set.

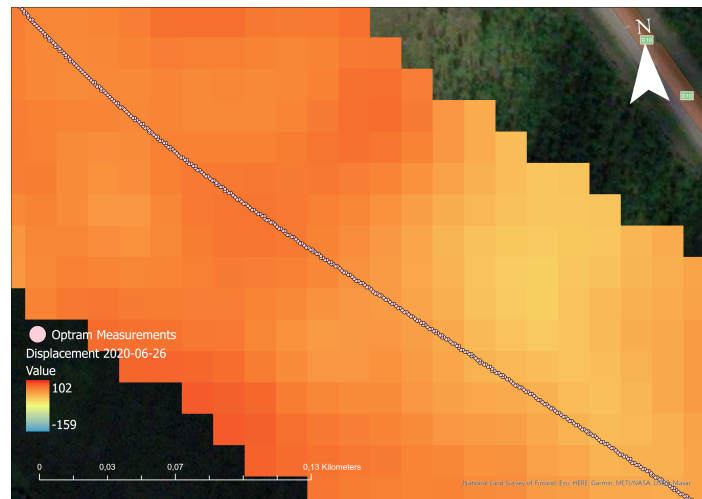


Figure 3.11: Optram measurements overlaid on InSAR raster. Optram points absorb the value of the InSAR they are located in.

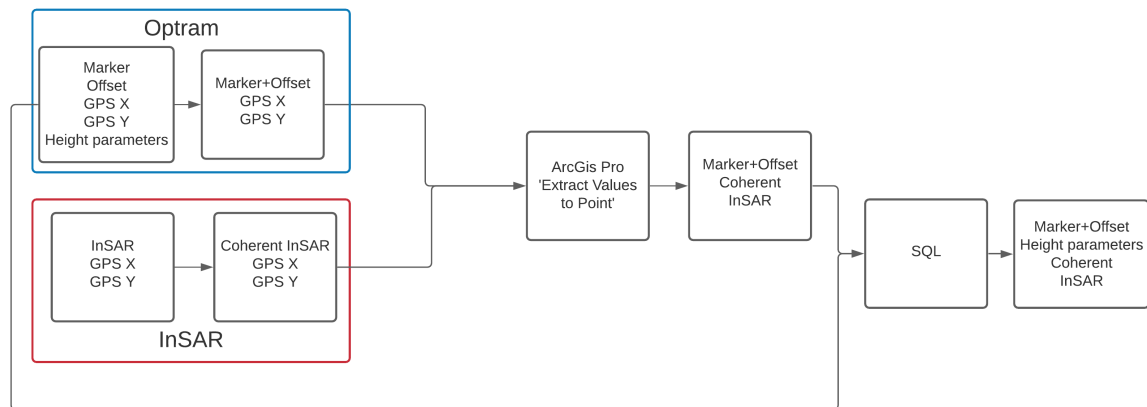


Figure 3.12: Flow chart for matching Optram measurements with InSAR measurements. GPS coordinates are used to match one Optram set and with all the InSAR measurements. Once this is done then all the other Optram series are attached with marker locations.

After the matching the data was reduced to only include measurements for whole meters. In order to do that SQL is used. Optram collects four measurements for every meter. These are each given an index i for every meter. Then every measurement with the index $i=1$ is selected for the next step (Figure 3.14). Figure 3.15 illustrated what a matched data sets look like.

Marker+Offset	Height Short-wave Left
1417874	0,1099
1417874,25	0,5099
1417874,5	0,8500
1417874,75	1,1100
1417875	1,2899
1417875,25	1,3999

↓

Marker+Offset	Height Short-wave Left	i
1417874	0,1099	1
1417874,25	0,5099	2
1417874,5	0,8500	3
1417874,75	1,1100	4
1417875	1,2899	1
1417875,25	1,3999	2

↓

Marker+Offset	Height Short-wave Left	i
1417874	0,1099	1
1417875	1,2899	1

Figur 3.13: Measurements from the same meter are ordered and assigned index i and the first i of every meter is selected. This results in one measurement per meter instead of four.

```

/* Assignment of i(1-4) to every 0.25 meter */
drop table if exists Optram_i
select *,ROW_NUMBER() over (partition by datum,am order by m) as i
into Optram_i
from Optram
-----
/* Selection of only the first i which is the whole meter*/
drop table if exists Optram_i_selected
select *
into Optram_i_selected
from Optram_i
where i=1

```

The result of the matching and aggregating is seen in figure 3.15.

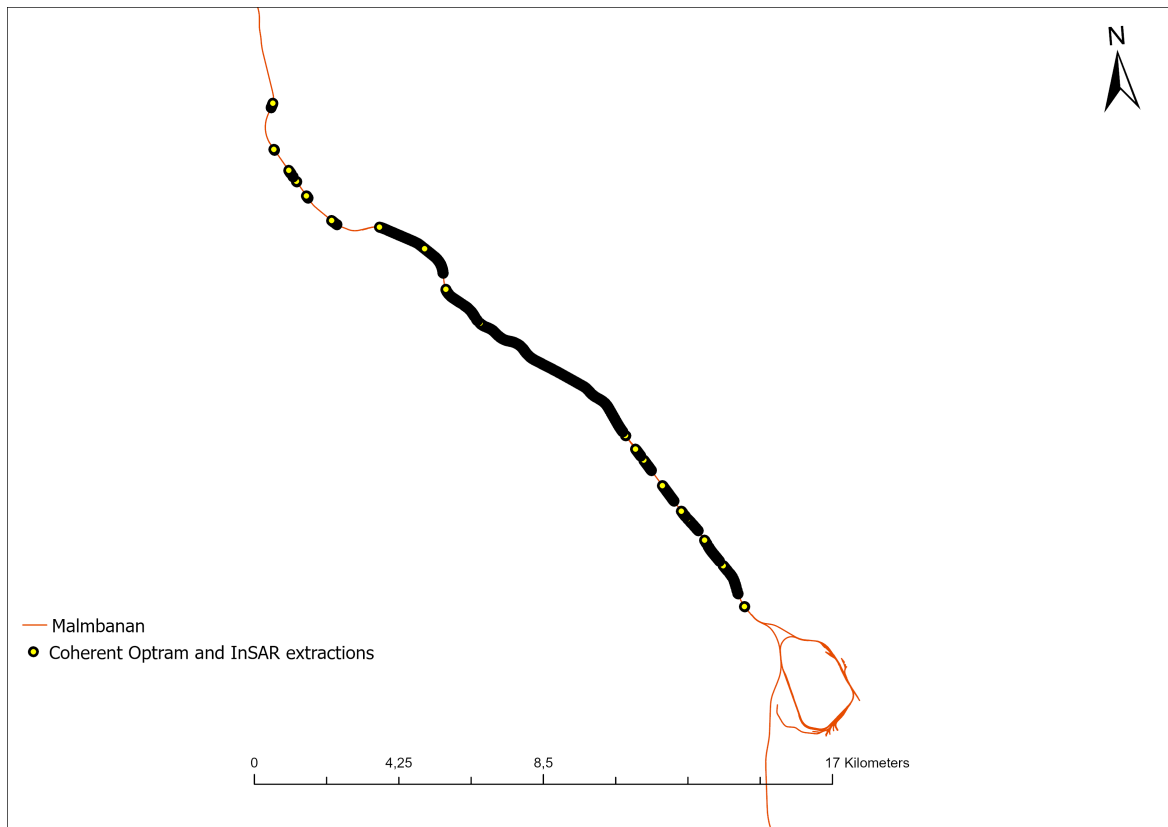


Figure 3.14: Point where Optram measurements overlap with with InSAR-derived displacement results having a coherency more than 0.5.

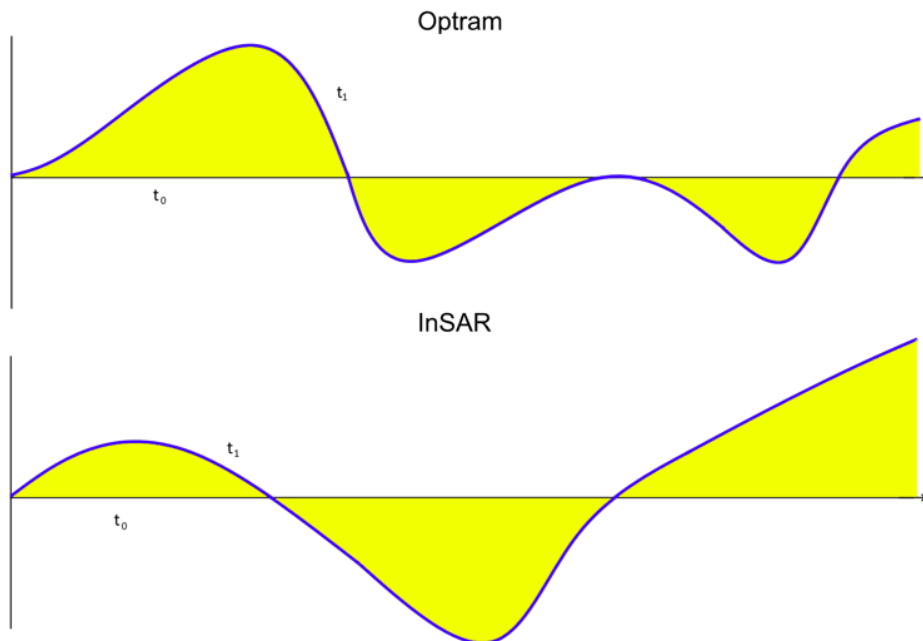
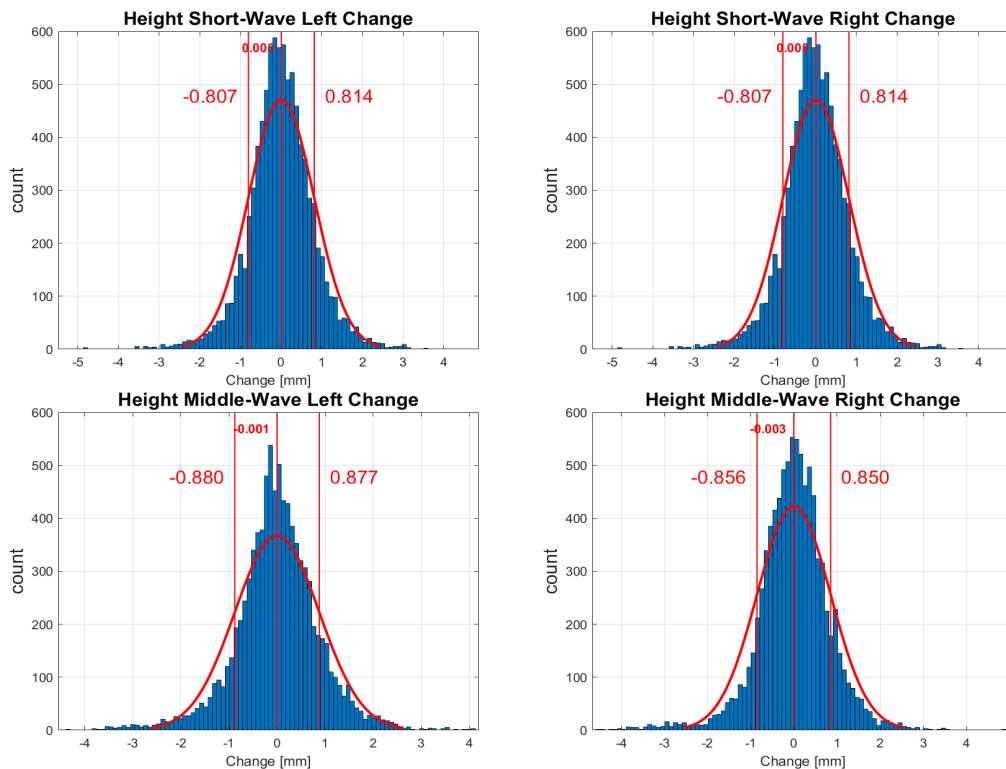


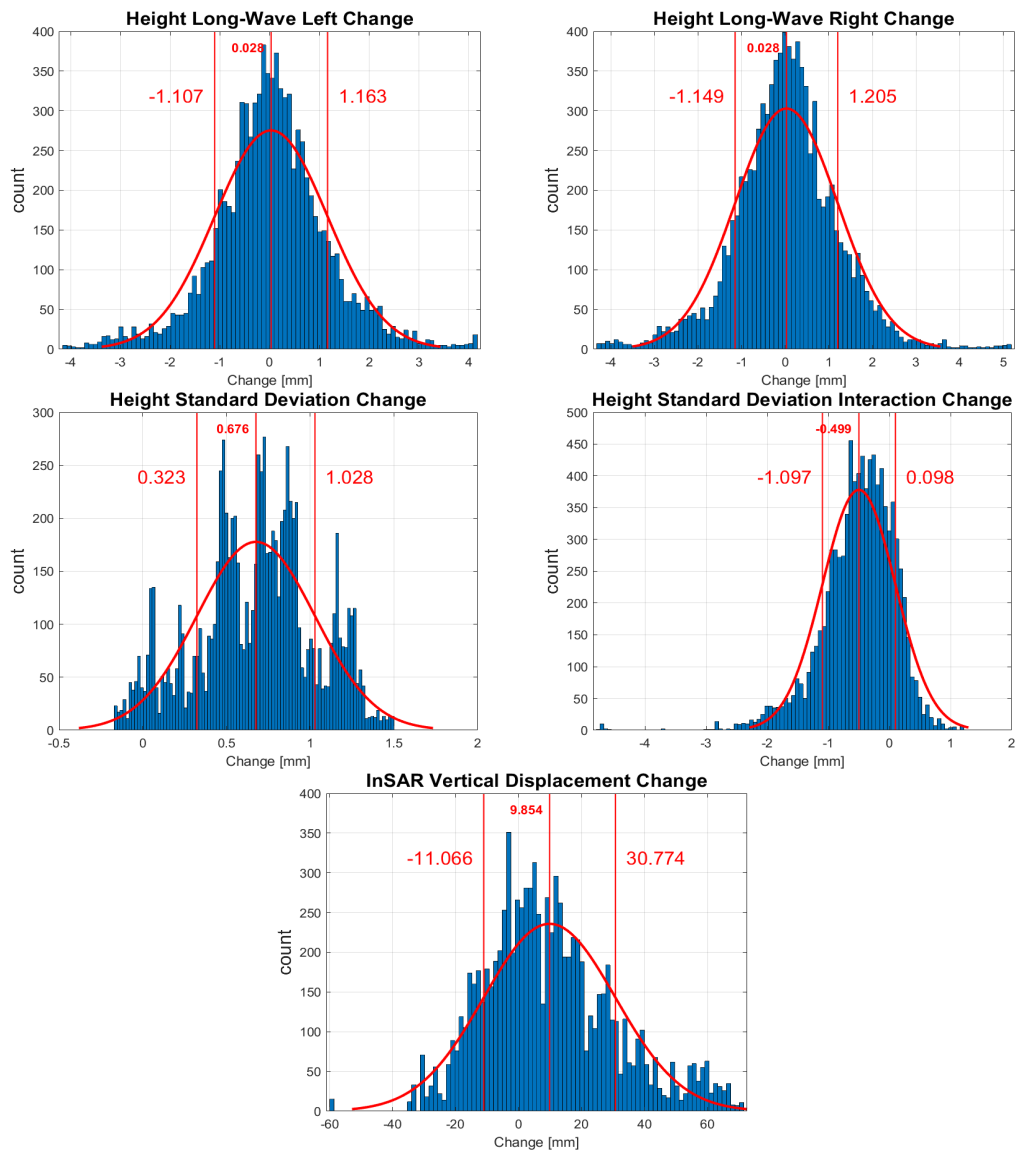
Figure 3.15: Illustration of matched data sets. The line t_0 indicated the values at the start of a time range while t_1 is the line for the end of the time range. These illustration are for understanding only and do not represent actual values.

3.5 Establishing threshold

Changes in Optram are compared with changes visible in InSAR. Measurements in Optram are absolute value. To get the change over time the end measurements are subtracted with the initial measurements. This will give us the change over the whole time frame. At some locations there will be small change and at other locations the change will be bigger. If the change for every parameter is plotted on a histogram and the mean and standard deviations are added, we are able to see that most changes are grouped around the mean. The objective is to see if locations with big changes in Optram and InSAR overlap. Therefore for every measured parameter the first and second standard deviations are treated as thresholds. Figure 3.16 and 3.17 shows the histograms and normal distribution lines for changes in test 1.



Figur 3.16: Distribution of change in measurements between 2015 and 2020 for four Optram parameters, the two vertical red lines are the first standard deviation.



Figur 3.17: Distribution of change for measurements between 2015 and 2020 for four Optram parameters and the InSAR displacement, the two vertical red lines are first the standard deviations.

3.6 Identify problematic areas

To identify problematic the points a SQL script is used. A *case* function will label all measurements that exceed thresholds as 1 and those that do not as 0 for all parameters. These measurements are then grouped together in sections of 25, 50 and 100 meters. If one measurement in a section exceeds the thresholds, the whole section will be labeled as exceeding the thresholds. In figure 3.18 thresholds have been added based on standard deviations and then every point exceeding the thresholds is marked as 1 and those not exceeding as 0.

```

case
    when abs([Height Short-Wave Left 2020] - [Height Short-Wave Left 2015])
        between -0.825 and 0.825 then 0
    else 1
end as [Height Short-Wave Left Parameter],
[. . .]
case when abs(InSAR2020-InSAR2015) between -11.066 and 30.774
    then 0
    else 1
end as [InSAR Parameter]

select
    Max([Height Short-Wave Left Parameter]) as HSWLsection,
[. . .]
    Max([InSAR Parameter]) as InSARsection
group by [50 Meter]

```

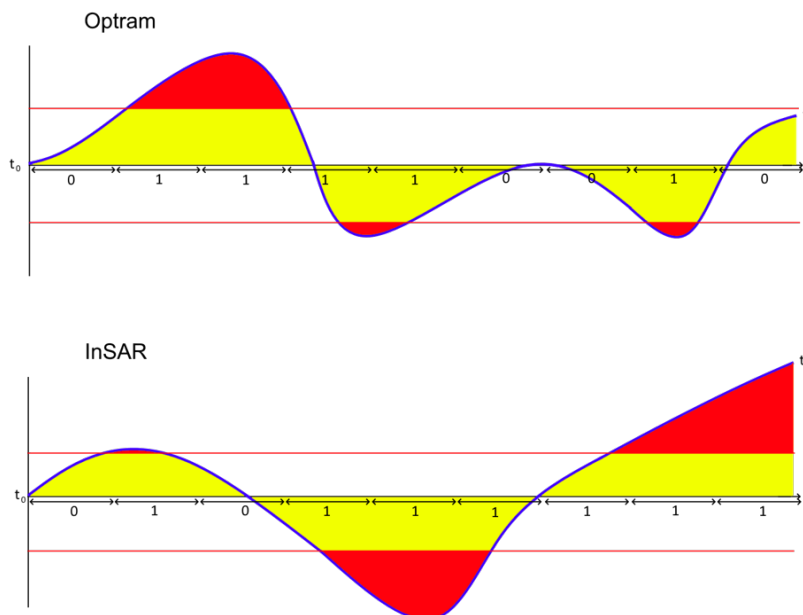


Figure 3.18: Point in Opram and InSAR that exceed the provided thresholds are marked as 1 and point that are within the thresholds are marked as 0.

3.7 Overlap

A *Case* function will look through all sections and see if there is any overlap between the Optram measurements that exceed the thresholds and the InSAR measurements that exceed thresholds. Then the *case* function will classify them into four categories in a confusion matrix (Figure 3.19).

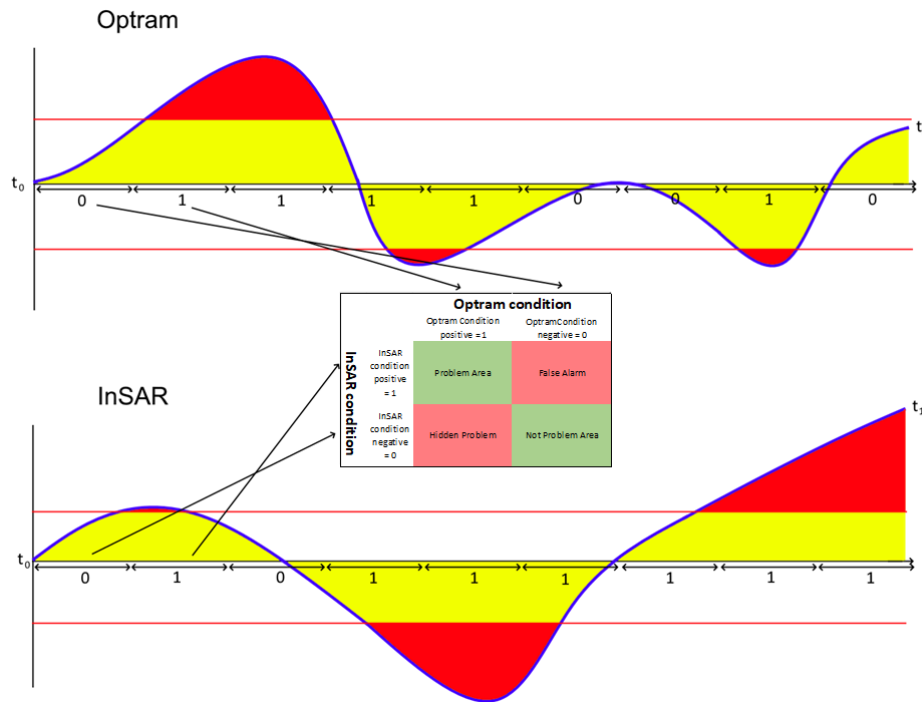


Figure 3.19: Modified confusion matrix. The green squares are areas where Optram and InSAR classification agree. The red squares are for areas where Optram and InSAR classification do not agree.

```

case
  when HSWLsection<>0 and InSARsection<>0 then 'Problem Area'
  when HSWLsection=0 and InSARsection<>0 then 'False Alarm'
  when HSWLsection<>0 and InSARsection=0 then 'Hidden Problem'
  when HSWLsection=0 and InSARsection=0 then 'Not Problem Area'
end as PresicionRecall

```

This script will count how many sections that belong to each category.

```

count(PresicionRecall) as TotalCount,
count(case PresicionRecall when 'Problem Area' then 1 else null end)
  as [Problem Area Count],
count(case PresicionRecall when 'False Alarm' then 1 else null end)
  as [False Alarm Count],
count(case PresicionRecall when 'Hidden Problem' then 1 else null end)
  as [Hidden Problem Count],
count(case PresicionRecall when 'Not Problem Area' then 1 else null end)
  as [Not Problem Area Count]

```

The *Problem Area* are sections where both the Optram parameter and InSAR exceed the thresholds. This means that the classification has been done correctly. The category *False Alarm* are sections where the Optram parameter does not exceed the threshold but InSAR does. *Hidden Problem* are sections where the Optram parameter exceed the thresholds but not for the InSAR parameter, these are problem sections that InSAR can't detect. *Not Problem Area* are sections where neither Optram parameter nor the InSAR parameter exceed thresholds. The performance of the classification is tested with a correlation score. Because we have the GPS coordinates for the measurements we are able to display the classification on map (Figure 3.20).

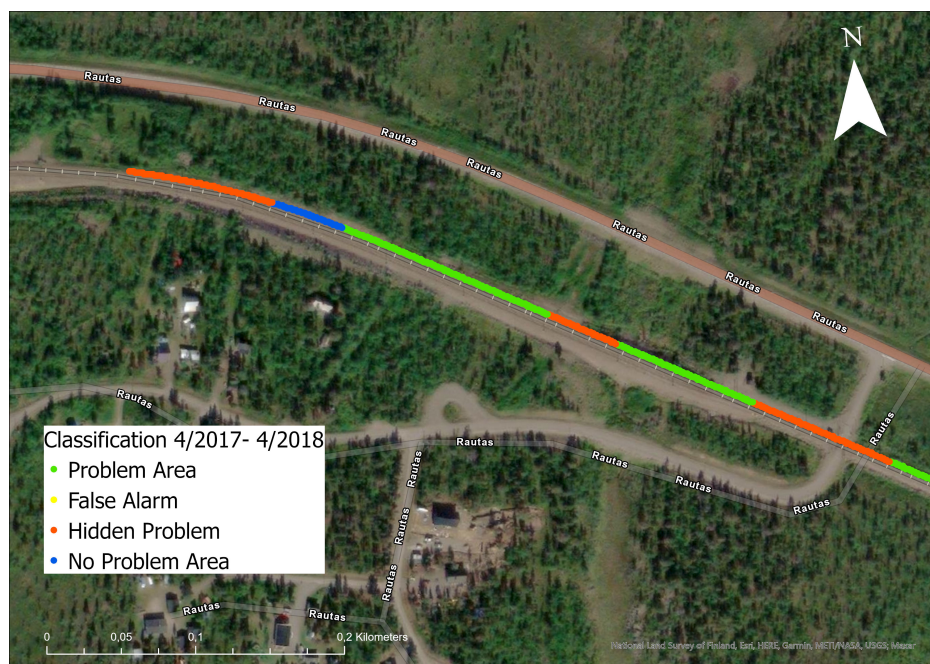


Figure 3.20: The classification displayed on a map

Correlation measures general overlap between Optram and InSAR. Higher correlation mean a higher rate of *Problem Area* and *Not Problem Area*, a higher correlation rate means higher conformity between Optram and InSAR. Two other measurements are used to see how the classification deals with *Hidden Problems* and *False Alarms*.

Correlation

$$\frac{\textit{Problem Area} + \textit{Not Problem Area}}{\textit{Total number of sections}}$$

Hidden Rate

$$\frac{\textit{Hidden Problem}}{\textit{Hidden Problem} + \textit{Problem Area}}$$

False Alarm Rate

$$\frac{\textit{False Alarm}}{\textit{False Alarm} + \textit{Not Problem Area}}$$

3.8 Sensitivity analyst

The project started of with substantial amount of raw data that had to be selected and processed. A sensitivity analysis looks at how different variables affect the outcome of the classification. In the sensitivity analysis variables are isolated and tested with different parameters to study how the results change.

4 Results and Analysis

In this chapter the results of the classifications for the different time ranges will be presented. The performance of the classification and a map for the overlap will be included.

4.1 Classification With Different Time Ranges

In this section the result for different time ranges are presented. These results were produced with the same section length and threshold selection method. 50 meter long sections with the first standard deviation being the threshold for all parameters. The correlation, hidden rate and false alarm rate is included to test the performance of the classification. Tables 4.1 and 4.2a shows the classification result for the longer time ranges and tables 4.2b,c,d,e is for a one year time ranges and table 4.2f is for 90 days time range. Generally the correlation score is slightly higher for shorter time frames. But the false alarm rate is also higher. The hidden rate is lower for shorter time frames. The correlation score is higher in the longer wavelengths for all time ranges except the 2016-2017, where shorter wavelength have a higher correlation.

12/2015-6/2020, 50 meter sections, 1st Standard Deviation							
Parameter	Problem Area	False Alarm	Hidden Problem	No Problem	Correlation	HR	FAR
Height Short-wave Left	43	2	147	11	0,27	0,77	0,15
Height Short-wave Right	44	1	147	10	0,27	0,77	0,09
Height Middle-wave Left	28	17	101	57	0,42	0,78	0,23
Height Middle-wave Right	26	19	103	55	0,40	0,80	0,26
Height Long-wave Left	22	23	74	84	0,52	0,77	0,21
Height Long-wave Right	23	22	77	81	0,51	0,77	0,21
Standard deviation Height	22	23	62	96	0,58	0,74	0,19
Standard Deviation Interaction	44	1	158	0	0,22	0,78	1,00

Tabell 4.1: Results for the longest time range, test 1 with the count of each quadrant of the classification and performance scores calculated with equations from chapter 3.7

4/2017-4/2020, 50 meter, 1st StDev				4/2016-4/2017, 50 meter, 1st StDev			
Parameter	Correlation	HR	FAR	Parameter	Correlation	HR	FAR
Height Short-wave Left	0,23	0,81	0,33	Height Short-wave Left	0,72	0,09	0,88
Height Short-wave Right	0,24	0,80	0,23	Height Short-wave Right	0,73	0,09	0,89
Height Middle-wave Left	0,49	0,77	0,17	Height Middle-wave Left	0,52	0,09	0,90
Height Middle-wave Right	0,46	0,80	0,20	Height Middle-wave Right	0,50	0,08	0,89
Height Long-wave Left	0,57	0,76	0,18	Height Long-wave Left	0,36	0,11	0,91
Height Long-wave Right	0,58	0,75	0,17	Height Long-wave Right	0,33	0,13	0,91
Standard deviation Height	0,56	0,74	0,15	Standard deviation Height	0,40	0,08	0,89
Standard Deviation Interaction	0,20	0,80	-	Standard Deviation Interaction	0,83	0,11	1,00

- (a) Test 2, three year time range from 2017 to 2020. (b) Test 3, one year time range from 2016 to 2017.

4/2017-4/2018, 50 meter, 1st StDev				4/2018-4/2019, 50 meter, 1st StDev			
Parameter	Correlation	HR	FAR	Parameter	Correlation	HR	FAR
Height Short-wave Left	0,43	0,58	0,47	Height Short-wave Left	0,39	0,66	0,38
Height Short-wave Right	0,44	0,57	0,38	Height Short-wave Right	0,40	0,65	0,32
Height Middle-wave Left	0,44	0,61	0,48	Height Middle-wave Left	0,49	0,68	0,37
Height Middle-wave Right	0,47	0,59	0,44	Height Middle-wave Right	0,52	0,66	0,35
Height Long-wave Left	0,48	0,62	0,45	Height Long-wave Left	0,55	0,68	0,35
Height Long-wave Right	0,51	0,58	0,43	Height Long-wave Right	0,53	0,70	0,37
Standard deviation Height	0,44	0,68	0,49	Standard deviation Height	0,62	0,62	0,34
Standard Deviation Interaction	0,42	0,58	-	Standard Deviation Interaction	0,67	0,48	0,29

- (c) Test 4, one year time range from 2017 to 2018. (d) Test 5, one year time range from 2018 to 2019.

4/2019-4/2020, 50 meter, 1st StDev				4/2020-6/2020, 50 meter, 1st StDev			
Parameter	Correlation	HR	FAR	Parameter	Correlation	HR	FAR
Height Short-wave Left	0,51	0,51	0,46	Height Short-wave Left	0,44	0,74	0,20
Height Short-wave Right	0,53	0,50	0,37	Height Short-wave Right	0,35	0,76	0,25
Height Middle-wave Left	0,53	0,50	0,34	Height Middle-wave Left	0,38	0,71	0,11
Height Middle-wave Right	0,54	0,48	0,43	Height Middle-wave Right	0,50	0,73	0,20
Height Long-wave Left	0,48	0,53	0,50	Height Long-wave Left	0,42	0,73	0,15
Height Long-wave Right	0,56	0,47	0,41	Height Long-wave Right	0,51	0,71	0,17
Standard deviation Height	0,48	0,52	-	Standard deviation Height	-	-	-
Standard Deviation Interaction	0,51	0,51	0,47	Standard Deviation Interaction	0,24	0,76	-

- (e) Test 6, one year time range from 2019 to 2020. (f) Test 7, 90 days time range from April 2020 to June 2020.

Tabell 4.2

4.2 Classification With Different Thresholds and Section Lengths

In tables 4.3-4.6 the difference in results can be seen when stricter thresholds have been implemented. In these results we can observe some patterns between different thresholds and section lengths. For all the time ranges (Table 4.3, 4.5, 4.6) except 2016-2017 (Table 4.4) applying a stricter threshold increases correlation. We can see that the hidden rate is higher with the second standard deviation threshold (Table 4.3b,d,f, 4.4b,d,f, 4.5b,d,f). For some time ranges there is a significant increase while for others there is a slight increase. Switching to the second standard deviation also decreases the false alarm rate for all time ranges (Table 4.3, 4.4, 4.5, 4.6).

Changing the length of the sections produces different results. For the first standard deviation using longer sections result in increasing correlation. Using longer sections with the second standard deviation results in slightly lower correlation.

12/2015-6/2020, 25 meter, 1st StDev				12/2015-6/2020, 25 meter, 2nd StDev			
Parameter	Correlation	HR	FAR	Parameter	Correlation	HR	FAR
Height Short-wave Left	0,29	0,80	0,14	Height Short-wave Left	0,61	0,92	0,07
Height Short-wave Right	0,29	0,79	0,11	Height Short-wave Right	0,58	0,95	0,08
Height Middle-wave Left	0,49	0,80	0,19	Height Middle-wave Left	0,79	0,97	0,08
Height Middle-wave Right	0,49	0,80	0,18	Height Middle-wave Right	0,81	0,94	0,07
Height Long-wave Left	0,55	0,81	0,20	Height Long-wave Left	0,83	0,95	0,07
Height Long-wave Right	0,54	0,82	0,21	Height Long-wave Right	0,84	0,92	0,07
Standard deviation Height	0,60	0,78	0,18	Standard deviation Height	0,91	1,00	0,07
Standard Deviation Interaction	0,19	0,81	--	Standard Deviation Interaction	0,27	0,95	0,13

(a) Test 8, 25 meter long sections with first standard deviation as threshold

(b) Test 9, 25 meter long sections with second standard deviation as threshold

12/2015-6/2020, 50 meter, 1st StDev				12/2015-6/2020, 50 meter, 2nd StDev			
Parameter	Correlation	HR	FAR	Parameter	Correlation	HR	FAR
Height Short-wave Left	0,27	0,77	0,15	Height Short-wave Left	0,51	0,92	0,08
Height Short-wave Right	0,27	0,77	0,09	Height Short-wave Right	0,42	0,95	0,12
Height Middle-wave Left	0,42	0,78	0,23	Height Middle-wave Left	0,75	0,95	0,09
Height Middle-wave Right	0,40	0,80	0,26	Height Middle-wave Right	0,75	0,93	0,08
Height Long-wave Left	0,52	0,77	0,21	Height Long-wave Left	0,79	0,96	0,09
Height Long-wave Right	0,51	0,77	0,21	Height Long-wave Right	0,80	0,93	0,08
Standard deviation Height	0,58	0,74	0,19	Standard deviation Height	0,90	1,00	0,08
Standard Deviation Interaction	0,22	0,78	1,00	Standard Deviation Interaction	0,18	0,94	0,19

(c) Test 10, 50 meter long sections with first standard deviation as threshold

(d) Test 11, 50 meter long sections with second standard deviation as threshold

12/2015-6/2020, 100 meter, 1st StDev				12/2015-6/2020, 100 meter, 2nd StDev			
Parameter	Correlation	HR	FAR	Parameter	Correlation	HR	FAR
Height Short-wave Left	0,26	0,74	-	Height Short-wave Left	0,36	0,89	0,09
Height Short-wave Right	0,27	0,74	0,00	Height Short-wave Right	0,29	0,90	0,12
Height Middle-wave Left	0,37	0,76	0,30	Height Middle-wave Left	0,64	0,91	0,11
Height Middle-wave Right	0,36	0,74	0,26	Height Middle-wave Right	0,68	0,90	0,11
Height Long-wave Left	0,48	0,75	0,27	Height Long-wave Left	0,75	0,94	0,11
Height Long-wave Right	0,50	0,72	0,22	Height Long-wave Right	0,78	0,88	0,10
Standard deviation Height	0,55	0,70	0,22	Standard deviation Height	0,87	1,00	0,11
Standard Deviation Interaction	0,26	0,74	-	Standard Deviation Interaction	0,13	0,92	0,33

(e) Test 12, 100 meter long sections with first standard deviation as threshold

(f) Test 13, 100 meter long sections with second standard deviation as threshold

Tabell 4.3: Results for the 12/2015-6/2020 time range with different thresholds and section lengths with only the performance scores

4/2016-4/2017, 25 meter, 1st StDev				4/2016-4/2017, 25 meter, 2nd StDev			
Parameter	Correlation	HR	FAR	Parameter	Correlation	HR	FAR
Height Short-wave Left	0,63	0,18	0,78	Height Short-wave Left	0,57	0,86	0,20
Height Short-wave Right	0,61	0,19	0,80	Height Short-wave Right	0,58	0,85	0,19
Height Middle-wave Left	0,47	0,17	0,79	Height Middle-wave Left	0,73	0,89	0,18
Height Middle-wave Right	0,46	0,16	0,78	Height Middle-wave Right	0,72	0,94	0,19
Height Long-wave Left	0,36	0,22	0,82	Height Long-wave Left	0,77	0,89	0,18
Height Long-wave Right	0,32	0,26	0,83	Height Long-wave Right	0,76	0,91	0,18
Standard deviation Height	0,41	0,16	0,79	Standard deviation Height	0,79	0,76	0,17
Standard Deviation Interaction	0,72	0,19	0,81	Standard Deviation Interaction	0,47	0,86	0,21

(a) Test 14, 25 meter long sections with first standard deviation as threshold

(b) Test 15, 25 meter long sections with second standard deviation as threshold

4/2016-4/2017, 50 meter, 1st StDev				4/2016-4/2017, 50 meter, 2nd StDev			
Parameter	Correlation	HR	FAR	Parameter	Correlation	HR	FAR
Height Short-wave Left	0,72	0,09	0,88	Height Short-wave Left	0,49	0,81	0,26
Height Short-wave Right	0,73	0,09	0,89	Height Short-wave Right	0,51	0,80	0,25
Height Middle-wave Left	0,52	0,09	0,90	Height Middle-wave Left	0,66	0,84	0,25
Height Middle-wave Right	0,50	0,08	0,89	Height Middle-wave Right	0,64	0,89	0,26
Height Long-wave Left	0,36	0,11	0,91	Height Long-wave Left	0,72	0,78	0,23
Height Long-wave Right	0,33	0,13	0,91	Height Long-wave Right	0,71	0,83	0,24
Standard deviation Height	0,40	0,08	0,89	Standard deviation Height	0,74	0,69	0,22
Standard Deviation Interaction	0,83	0,11	1,00	Standard Deviation Interaction	0,33	0,83	0,35

(c) Test 16, 50 meter long sections with first standard deviation as threshold

(d) Test 17, 50 meter long sections with second standard deviation as threshold

4/2016-4/2017, 100 meter, 1st StDev				4/2016-4/2017, 100 meter, 2nd StDev			
Parameter	Correlation	HR	FAR	Parameter	Correlation	HR	FAR
Height Short-wave Left	0,83	0,05	0,93	Height Short-wave Left	0,46	0,71	0,30
Height Short-wave Right	0,82	0,06	0,93	Height Short-wave Right	0,46	0,72	0,31
Height Middle-wave Left	0,68	0,04	0,91	Height Middle-wave Left	0,58	0,78	0,32
Height Middle-wave Right	0,62	0,05	0,93	Height Middle-wave Right	0,55	0,86	0,34
Height Long-wave Left	0,46	0,06	0,95	Height Long-wave Left	0,67	0,70	0,29
Height Long-wave Right	0,40	0,07	0,95	Height Long-wave Right	0,64	0,82	0,31
Standard deviation Height	0,48	0,02	0,92	Standard deviation Height	0,70	0,50	0,27
Standard Deviation Interaction	0,90	0,06	1,00	Standard Deviation Interaction	0,32	0,74	0,43

(e) Test 18, 100 meter long sections with first standard deviation as threshold

(f) Test 19, 100 meter long sections with second standard deviation as threshold

Tabell 4.4: Results for the 4/2016-4/2017 time range with different thresholds and section lengths with only the performance scores

4/2017-4/2018, 25 meter, 1st StDev				4/2017-4/2018, 25 meter, 2nd StDev			
Parameter	Correlation	HR	FAR	Parameter	Correlation	HR	FAR
Height Short-wave Left	0,45	0,62	0,38	Height Short-wave Left	0,69	0,91	0,07
Height Short-wave Right	0,41	0,65	0,33	Height Short-wave Right	0,66	0,94	0,08
Height Middle-wave Left	0,48	0,66	0,36	Height Middle-wave Left	0,80	0,98	0,08
Height Middle-wave Right	0,49	0,66	0,36	Height Middle-wave Right	0,80	0,96	0,08
Height Long-wave Left	0,51	0,70	0,37	Height Long-wave Left	0,81	1,00	0,08
Height Long-wave Right	0,53	0,68	0,36	Height Long-wave Right	0,81	1,00	0,09
Standard deviation Height	0,51	0,73	0,38	Standard deviation Height	0,87	1,00	0,08
Standard Deviation Interaction	0,34	0,66	-	Standard Deviation Interaction	0,28	0,93	0,08

(a) Test 20, 25 meter long sections with first standard deviation as threshold

(b) Test 21, 25 meter long sections with second standard deviation as threshold

4/2017-4/2018, 50 meter, 1st StDev				4/2017-4/2018, 50 meter, 2nd StDev			
Parameter	Correlation	HR	FAR	Parameter	Correlation	HR	FAR
Height Short-wave Left	0,43	0,58	0,47	Height Short-wave Left	0,59	0,90	0,08
Height Short-wave Right	0,44	0,57	0,38	Height Short-wave Right	0,52	0,94	0,11
Height Middle-wave Left	0,44	0,61	0,48	Height Middle-wave Left	0,72	0,98	0,10
Height Middle-wave Right	0,47	0,59	0,44	Height Middle-wave Right	0,75	0,95	0,10
Height Long-wave Left	0,48	0,62	0,45	Height Long-wave Left	0,77	1,00	0,10
Height Long-wave Right	0,51	0,58	0,43	Height Long-wave Right	0,75	1,00	0,11
Standard deviation Height	0,44	0,68	0,49	Standard deviation Height	0,85	1,00	0,09
Standard Deviation Interaction	0,42	0,58	-	Standard Deviation Interaction	0,19	0,92	0,14

(c) Test 22, 50 meter long sections with first standard deviation as threshold

(d) Test 23, 50 meter long sections with second standard deviation as threshold

4/2017-4/2018, 100 meter, 1st StDev				4/2017-4/2018, 100 meter, 2nd StDev			
Parameter	Correlation	HR	FAR	Parameter	Correlation	HR	FAR
Height Short-wave Left	0,53	0,46	1,00	Height Short-wave Left	0,49	0,89	0,08
Height Short-wave Right	0,54	0,45	--	Height Short-wave Right	0,42	0,92	0,11
Height Middle-wave Left	0,51	0,46	0,56	Height Middle-wave Left	0,64	0,97	0,12
Height Middle-wave Right	0,49	0,48	0,64	Height Middle-wave Right	0,66	0,96	0,12
Height Long-wave Left	0,49	0,47	0,55	Height Long-wave Left	0,75	1,00	0,11
Height Long-wave Right	0,49	0,47	0,55	Height Long-wave Right	0,73	1,00	0,11
Standard deviation Height	0,43	0,53	0,61	Standard deviation Height	0,84	1,00	0,10
Standard Deviation Interaction	0,54	0,46	-	Standard Deviation Interaction	0,11	0,91	0,25

(e) Test 24, 100 meter long sections with first standard deviation as threshold

(f) Test 25, 100 meter long sections with second standard deviation as threshold

Tabell 4.5: Results for the 4/2017-4/2018 time range with different thresholds and section lengths with only the performance scores

4/2020-6/2020, 25 meter, 1st StDev				4/2020-6/2020, 25 meter, 2nd StDev			
Parameter	Correlation	HR	FAR	Parameter	Correlation	HR	FAR
Height Short-wave Left	0,53	0,73	0,17	Height Short-wave Left	0,86	0,84	0,04
Height Short-wave Right	0,43	0,76	0,20	Height Short-wave Right	0,80	0,97	0,00
Height Middle-wave Left	0,45	0,73	0,13	Height Middle-wave Left	0,85	0,73	0,00
Height Middle-wave Right	0,56	0,74	0,20	Height Middle-wave Right	0,98	0,00	0,02
Height Long-wave Left	0,50	0,73	0,16	Height Long-wave Left	1,00	0,04	0,00
Height Long-wave Right	0,58	0,71	0,17	Height Long-wave Right	0,98	0,00	0,02
Standard deviation Height	-	-	-	Standard deviation Height	-	-	-
Standard Deviation Interaction	0,22	0,78	-	Standard Deviation Interaction	0,06	0,94	0,00

(a) Test 26, 25 meter long sections with first standard deviation as threshold

(b) Test 27, 25 meter long sections with second standard deviation as threshold

4/2020-6/2020, 50 meter, 1st StDev				4/2020-6/2020, 50 meter, 2nd StDev			
Parameter	Correlation	HR	FAR	Parameter	Correlation	HR	FAR
Height Short-wave Left	0,44	0,74	0,20	Height Short-wave Left	0,82	0,82	0,05
Height Short-wave Right	0,35	0,76	0,25	Height Short-wave Right	0,78	0,75	0,00
Height Middle-wave Left	0,38	0,71	0,11	Height Middle-wave Left	0,77	0,75	0,00
Height Middle-wave Right	0,50	0,73	0,20	Height Middle-wave Right	0,96	0,00	0,04
Height Long-wave Left	0,42	0,73	0,15	Height Long-wave Left	0,99	0,17	0,00
Height Long-wave Right	0,51	0,71	0,17	Height Long-wave Right	0,96	0,00	0,04
Standard deviation Height	-	-	-	Standard deviation Height	-	-	-
Standard Deviation Interaction	0,24	0,76	-	Standard Deviation Interaction	0,07	0,93	-

(c) Test 28, 50 meter long sections with first standard deviation as threshold

(d) Test 29, 50 meter long sections with first standard deviation as threshold

4/2020-6/2020, 100 meter, 1nd StDev				4/2020-6/2020, 100 meter, 2nd StDev			
Parameter	Correlation	HR	FAR	Parameter	Correlation	HR	FAR
Height Short-wave Left	0,44	0,68	0,19	Height Short-wave Left	0,76	0,79	0,12
Height Short-wave Right	0,33	0,72	--	Height Short-wave Right	0,70	0,70	0,00
Height Middle-wave Left	0,36	0,69	0,10	Height Middle-wave Left	0,69	0,70	0,00
Height Middle-wave Right	0,49	0,67	0,20	Height Middle-wave Right	0,92	0,00	0,08
Height Long-wave Left	0,35	0,71	0,23	Height Long-wave Left	0,99	0,07	0,00
Height Long-wave Right	0,45	0,68	0,19	Height Long-wave Right	0,92	0,00	0,08
Standard deviation Height	-	-	-	Standard deviation Height	-	-	-
Standard Deviation Interaction	0,29	0,71	-	Standard Deviation Interaction	0,13	0,87	-

(e) Test 30, 100 meter long sections with first standard deviation as threshold

(f) Test 31, 100 meter long sections with second standard deviation as threshold

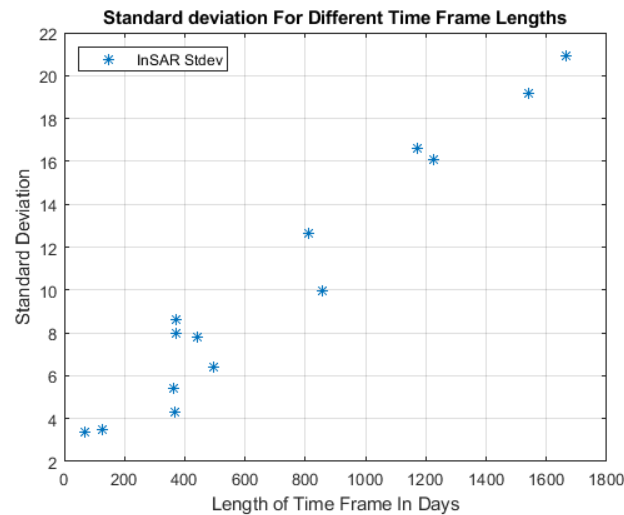
Tabell 4.6: Results for the 4/2017-4/2018 time range with different thresholds and section lengths with only the performance scores. Some scores are missing because threshold could not be established for standard deviation height

5 Discussion

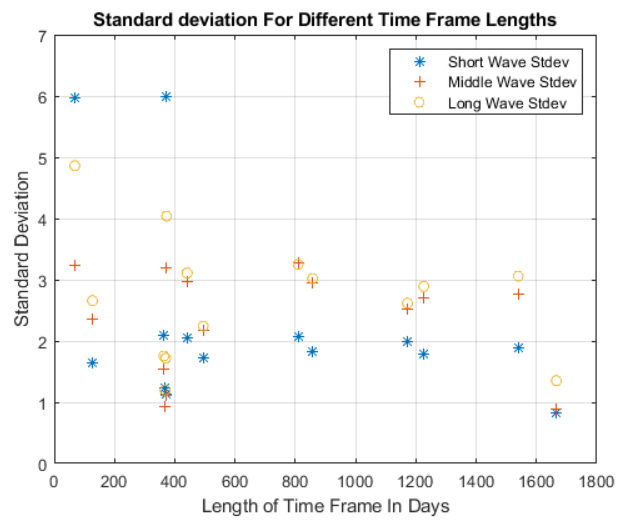
In this chapter the results are discussed. What causes different result among the different tests. A section related to error sources is also presented.

5.1 Effect of Time Frames

Reducing the length of the time frame generally increases the performance of the classification. This might be because of less decorrelation over shorter time ranges. As can be seen in graph 5.1 standard deviation for changes in InSAR decreases significantly with shorter time ranges, while it remains almost constant with changes in Optram (Figure 5.2). This would indicate that the use of smaller standard deviation as thresholds lead to higher correlation.



Figur 5.1: The standard deviation of displacement increases with longer time frame for InSAR. As the time range increases changes become more spread.



Figur 5.2: The standard deviation is almost constant with longer time frame for Optram. Even with longer time ranges the spread remains almost the same.

5.2 Selection of Thresholds

When using stricter thresholds, the result of classification change. This indicates that Optram and InSAR measurements are effected differently by the stricter thresholds. If the effect of stricter thresholds would have been the same for Optram and InSAR then the correlation score would have remained the same. Figure 5.3 show how different thresholds apply to the same data set. Stricter thresholds generally increases correlation but also significantly increases hidden rate.

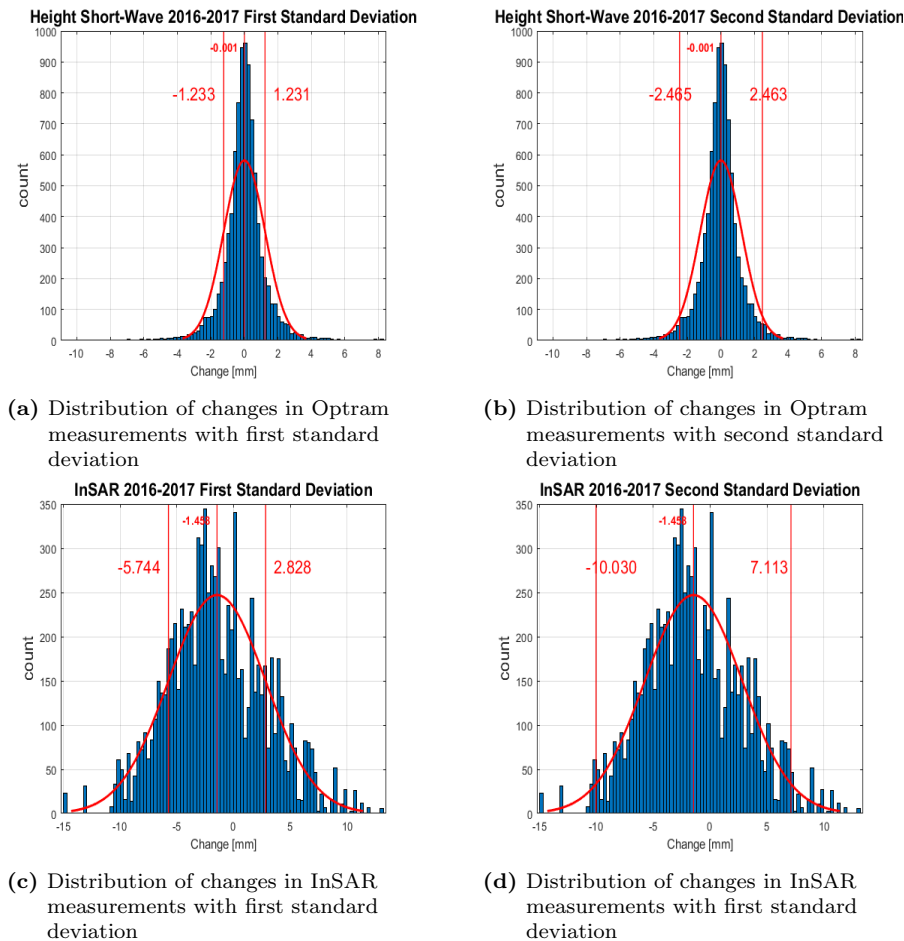


Figure 5.3: Distribution of changes in InSAR is less asymmetrical and therefore changes in threshold selection might cause a different result

5.3 Aggregation Length

At first glance, classification with longer section length indicates better performance. But once the loss of detail is considered, it becomes apparent that longer sections do not give a better picture for track condition monitoring. As mentioned before this is mainly due to the allowance for longer search distances between infractions in Optram and InSAR. This results in higher correlation but also the risk that these infractions are offset by a larger distance.

5.4 Sources of Error

Effect of Low Coherence

As mentioned in the section about InSAR, high decorrelation lead to low coherence and low coherence makes poor deformation detection. In the method the cut-of for usable points was a coherence index of 0.5. This meant that almost 92 % of all InSAR ground points were removed from the data set. This left mostly points with coherence between 0.5 and 0.55 which is considered barely acceptable. The correlation of the remaining points might not be high enough for comparison with a highly accurate and precise monitoring system like Optram. Other studies have used higher coherence thresholds, such as 0.7 (Bakon et al, 2016).

Differences in resolution

Optram and InSAR measure two different things. Optram measure the height of the rail with a 25 centimeter interval, meanwhile InSAR, measure ground deformation with a 15x15 meter cell (Figure 5.4). This ground cell is affected by every scattered inside and not just the rails. This means that the deformation for the rail might be different than for the whole cell. For example, the track is protected against frost heave but the surrounding ground isn't. Therefore InSAR cells that include the track are affected by frost heave while the track itself isn't.



Figur 5.4: The red line is the rail that the Optram measurement while InSAR measures the whole image (Müseler, 2018)

5.5 Method discussion

Using InSAR to measure ground displacement is not something new. But using it for railway track condition monitoring and comparing it to conventional technologies is. When planing the method for this study, there was no prior established methodology to follow or to replicate. Therefore the method that was devised for this study is considered unproven. Because of this it is difficult to determined if the method is reasonable or if the results can be trusted. For this study assumption were made about the selections of parameters and thresholds, for a master student with little prior knowledge and experience in SAR measurements and track maintenance it is difficult to determine what assumptions and selections of thresholds are reasonable to make. Even the way in which to present the results is unknown.

6 Conclusion

The purpose of this thesis is to study the use of InSAR for track condition monitoring and evaluate it by practicality and consistency. For this thesis, measurements from Malmbanan in northern Sweden were with a classification model as a case study. This classification model tries to find overlap between changes in Optram and InSAR.

The analysis showed that InSAR for track condition monitoring is affected too much by involved parameters for us to draw a clear conclusion. Although there seems to be some connection between InSAR and Optram measurements, as seen in the results, the connection is still very unclear with so much variation in correlation, hidden problem sections and false alarms. These performance scores often work in contradiction with each other, improving one score lead to degradation of another score.

The results and analysis, highlights the capabilities and limitations for track condition monitoring with SBAS time series technique. To much inconsistency across different time ranges when other parameters are kept the same. In order to reach a high correlation score, one must also accept high hidden rate or high false alarm rate. The situation were a choice has to been made between high hidden problem rate or high false alarm rate, makes it in the current state not practically viable for regular track condition monitoring.

6.1 Future research

For future research about InSAR for track condition monitoring one should focus on time series techniques that provide higher coherence. Time series InSAR techniques such a persistent scattering interferometry could provide higher coherence but also focuses more on scatter from man-made structures like railroads.

7 References

7.1 Literature

Ager, T. (2013). An introduction to synthetic aperture radar imaging. *Oceanography*, vol. 26, no. 2, DOI:10.5670/oceanog.2013.28.

Allen, M.R., O.P. Dube, W. Solecki, F. Aragón-Durand, W. Cramer, S. Humphreys, M. Kainuma, J. Kala, N. Mahowald, Y. Mulugetta, R. Perez, M. Wairiu, and K. Zickfeld, 2018: Framing and Context. In: Global Warming of 1.5°C. An IPCC Special Report on the impacts of global warming of 1.5°C above pre-industrial levels and related global greenhouse gas emission pathways, in the context of strengthening the global response to the threat of climate change, sustainable development, and efforts to eradicate poverty [Masson-Delmotte, V., P. Zhai, H.-O. Pörtner, D. Roberts, J. Skea, P.R. Shukla, A. Pirani, W. Moufouma-Okia, C. Péan, R. Pidcock, S. Connors, J.B.R. Matthews, Y. Chen, X. Zhou, M.I. Gomis, E. Lonnoy, T. Maycock, M. Tignor, and T. Waterfield (eds.)]. In Press.

Campbell, J., Wynne, R. (2011). Introduction to Remote Sensing, New York: The Guilford Press

Chang, L., Dollevoet, R., Hanssen, R.F., (2014). Railway infrastructure monitoring using satellite radar data, *International Journal of Railway Technology*, vol. 3, no. 2, DOI:10.4203/ijrt.3.2.5

Chinowsky, P., Helman, J., Gulati, S., Neumann, J., Martinich, J. (2019). Impacts of climate change on operation of the US rail network, *Transport Policy*, vol. 3, no. 2, DOI:10.1016/j.tranpol.2017.05.007

Sami, S.E. (2017). Exploitation of distributed scatterers in synthetic aperture radar interferometry. PhD thesis, Department of Geoscience and Remote-Sensing (GRS), Delft University of Technology, Delft.

Guoqing, Y., Jingqin, M. (2008). D-InSAR Technique for Land Subsidence Monitoring, *EARTH SCIENCE FRONTIERS*, vol. 15, no. 4, DOI:10.1016/S1872-5791(08)60059-7

Hanssen, R. (2002). Remote Sensing and Digital Image Processing, Dordrecht: Kluwer Academic Publishers

Hjort, J., Karjalainen O., Aalto, J., Westermann, S., Romanovsky, V.E., Nelson, F.E., Etzelmüller, B., Louto, M., (2018). 'Degrading permafrost puts Arctic infrastructure at risk by mid-century', DOI:10.1038/s41467-018-07557-4

- Hooper, A., Segall, P., Zebker H. (2007). Persistent scatterer interferometric synthetic aperture radar for crustal deformation analysis, with application to Volcán Alcedo, Galápagos, *JOURNAL OF GEOPHYSICAL RESEARCH*, vol. 112, DOI:10.1029/2006JB004763
- Lillesand, T.M., Kiefer, R.W., Chipman, J.W. (2015). Remote Sensing and Image Interpretation. Hoboken: John Wiley Sons
- Minh, D., Hanssen, R. Rocca, F. (2020). Radar Interferometry: 20 Years of Development in Time Series Techniques and Future Perspectives, *Remote Sens*, vol. 9, DOI:10.3390/rs12091364
- Moreira, A., Prats-Iraola, P., Yoiunis, M., Krieger, G., Hajnsek, I., Papathanassiou, K., (2013). A Tutorial on Synthetic Aperture Radar, *IEEE Geoscience and Remote Sensing Magazine*, vol. 1, no. 1, DOI:10.1109/MGRS.2013.2248301
- Pawluszek-Filipiak, K., Borkowski, A. (2020). Integration of DInSAR and SBAS Techniques to Determine Mining-Related Deformations Using Sentinel-1 Data: The Case Study of Rydułtowy Mine in Poland. *Remote Sens*, vol. 12, no. 2, DOI:10.3390/rs12020242
- Peterson, T., McGuirk, M., Houston T.G., Horvitz, A.H., Wehner, M.F., (2008). 'Climate variability and change with implications for transportation',
- Rossetti, M., (2003). 'Potential Impacts of Climate Change on Railroads'.
- SIS, (2019). Railway applications – Track – Track geometry quality – Part 1: Characterization of track geometry, SS-EN 13848-1. Stockholm: Swedish Standards Institute
- SMHI, (2020). Månads-, årstids- och årskartor. <https://www.smhi.se/data/meteorologi/kartor/>
- Tosti, F., Gagliardi, V., D'amico, F., Alani, A.M., (2020). 'Transport infrastructure monitoring by data fusion of GPR and SAR imagery information', *Transportation Research Procedia*, 45, DOI:10.1016/j.trpro.2020.02.097Get
- Trafikverket, (2020). TRVINFRA-00013. Borlänge: Trafikverket
- Trafikverket, (2021a). Optram. <https://www.trafikverket.se/tjanster/system-och-verktyg/forvaltning-och-underhall/Optram/>
- Trafikverket, (2021b). Malmbanan. <https://www.trafikverket.se/nara-dig/Norrbotten/vi-bygger-och-forbattrar/Malmbanan/>
- Yang, Z, (2015). Monitoring and Predicting Railway Subsidence Using InSAR and Time Series Prediction Techniques, PhD thesis, The University of Birmingham, Birmingham.
- Yhokha, A., Goswami, P.K., Chang, CP., Yen, JY., Ching, KE., Aruche, K.M. (2018). Application of Persistent Scatterer Interferometry (PSI) in monitoring slope movements in Nainital, Uttarakhand Lesser Himalaya, *Journal of Earth System Science*, vol. 127, DOI:10.1007/s12040-017-0907-y

7.2 Images

RCraig, 2020. *Synthetic Aperture Radar*.

CC BY-SA 4.0 licence

Available at :https://commons.wikimedia.org/wiki/File:Synthetic_Aperture_Radar.svg

Moscote, Anthony David Atencio. 2016. *Precision-Accuracy*.

CC BY-SA 4.0 licence

Available at :<https://commons.wikimedia.org/wiki/File:Precision-Accuracy.svg>

Müseler, Arne. 2018 *Puch tracks gleise*.

www.arne-mueseler.com, CC-BY-SA-3.0 licence, modified

Available at :https://commons.wikimedia.org/wiki/File:Puch_tracks_gleise.jpg

